

ELECTROSTATIC MECHANISM OF EMISSION ENHANCEMENT IN  
HYBRID METAL-SEMICONDUCTOR LIGHT-EMITTING  
HETEROSTRUCTURES

Antonio Llopis, B.S., M.S.

Dissertation Prepared for the Degree of  
DOCTOR OF PHILOSOPHY

UNIVERSITY OF NORTH TEXAS

May 2012

APPROVED:

Arup Neogi, Major Professor  
Arkadii Krokhin, Committee Member  
Tae-Youl Choi, Committee Member  
Zygmunt Gryczynski, Committee  
Member  
David Schultz, Chair of the Department  
of Physics  
James D. Meernik, Acting Dean of the  
Toulouse Graduate School

Llopis, Antonio. Electrostatic mechanism of emission enhancement in hybrid metal-semiconductor light-emitting heterostructures. Doctor of Philosophy (Physics), May 2012, 96 pp., 5 tables, 34 illustrations, references, 72 titles.

III-V nitrides have been put to use in a variety of applications including laser diodes for modern DVD devices and for solid-state white lighting. Plasmonics has come to the foreground over the past decade as a means for increasing the internal quantum efficiency (IQE) of devices through resonant interaction with surface plasmons which exist at metal/dielectric interfaces. Increases in emission intensity of an order of magnitude have been previously reported using silver thin-films on InGaN/GaN MQWs. The dependence on resonant interaction between the plasmons and the light emitter limits the applications of plasmonics for light emission.

This dissertation presents a new non-resonant mechanism based on electrostatic interaction of carriers with induced image charges in a nearby metallic nanoparticle. Enhancement similar in strength to that of plasmonics is observed, without the restrictions imposed upon resonant interactions. In this work we demonstrate several key features of this new interaction, including intensity-dependent saturation, increase in the radiative recombination lifetime, and strongly inhomogeneous light emission. We also present a model for the interaction based on the aforementioned image charge interactions. Also discussed are results of work done in the course of this research resulting in the development of a novel technique for strain measurement in light-emitting structures. This technique makes use of a spectral fitting model to extract information about electron-phonon interactions in the sample which can then be related to strain using theoretical modeling.

Copyright 2012

by

Antonio Llopis

## ACKNOWLEDGEMENTS

Thanks to my wife, Gosia, for her support in this endeavor. Thanks to my advisor and mentor in all things experimental, Dr. Arup Neogi, and to Dr. Arkadii Krokhin, who has served as a mentor for my theoretical and modeling work. Thanks to Dr. Sergio Pereira for providing the samples that made this work possible, and for the many informative discussions we had while trying to understand this effect. Thanks to fellow student Jie Lin, whose expertise in experiments far exceeds my own, and whose help was invaluable in retrieving high-quality experimental data for this work.

A special thanks also goes to the Doctors Gryczynski, Karol and Ignacy, at the UNT Health Sciences center for graciously allowing us to use their facilities for FLIM, AFM and time-resolved measurements on several occasions. Also to Ryan Rich there for his help in acquiring the FLIM images I made use of in Chapter 5.

Further thanks go to Dr. Motoichi Ohtsu at the University of Tokyo for hosting me for two months and allowing me to make use of their world-class NSOM equipment. Also to Dr. Tadashi Kawazoe, from whom I learned more in two months regarding the NSOM than I managed to learn in two years of playing with the instrument.

A final, personal thanks to Dr. Wayne Zimmerman, Dr. Mark Hamner and (now) Dr. Lindsay Renfro, who, while not involved in this work, helped me discover the love of research that led me down this path.

# TABLE OF CONTENTS

	Page
ACKNOWLEDGEMENTS .....	iii
LIST OF TABLES .....	vi
LIST OF FIGURES .....	vii
CHAPTER 1: INTRODUCTION.....	1
1.1 Semiconductors and Light Emission .....	1
1.2 Plasmonics .....	1
1.3 Non-resonant Enhancement and Strain Mapping .....	3
CHAPTER 2: III-V NITRIDES .....	5
2.1 Introduction to Nitrides .....	5
2.2 Tertiary Compounds and Heterostructures .....	7
2.3 Growth Issues and Defects .....	8
2.3.1 Epitaxial Layer Over-Growth .....	9
2.3.2 Inverted Hexagonal Pits and TDs.....	10
2.4 Piezoelectricity and the Quantum-Confined Stark Effect .....	14
2.5 Electron-Phonon Interactions and Phonon Replicas.....	16
CHAPTER 3: EXPERIMENTAL METHODS.....	18
3.1 Introduction .....	18
3.2 Origin of Luminescence .....	18
3.3 Far-field vs. Near-field.....	20
3.4 Far-field PL .....	21
3.4.1 Temperature Dependent PL.....	22
3.4.2 Angle-Dependent PL.....	24
3.5 Time-resolved PL.....	25
3.5.1 Power-Dependent TRPL .....	26
3.6 Near-field PL .....	27
3.7 Fitting Spectra.....	29
3.8 Fitting TRPL Decay Measurements .....	32

CHAPTER 4: SPECTRAL STRAIN MAPPING.....	35
4.1    Introduction .....	35
4.2    The Huang-Rhys Parameter (S) .....	36
4.3    Calculating S.....	37
4.3.1    The Exciton Wavefunction .....	38
4.3.2    The Phonon Dispersion Relation.....	44
4.3.3 $\mathcal{A}_j\mathcal{B}_j$ – The Interface Constants .....	47
4.3.4 $\Gamma$ – The Electron-Phonon Coupling Strength.....	48
4.4    S and Strain .....	51
4.5    Application: Near-field Strain Mapping.....	53
4.6    Summary and Future Work.....	57
CHAPTER 5: THE IMAGE CHARGE EFFECT .....	59
5.1    Emission Enhancement and Applied Plasmonics .....	59
5.2    Anomalous Photoluminescence Results.....	60
5.3    The Image Charge Effect.....	61
5.4    Modeling the Image Charge Effect .....	64
5.5    Power Saturation and Screening .....	68
5.6    Angle Dependent PL Measurements .....	73
5.7    Modification of Electron-Phonon Coupling .....	75
5.8    Near-field Spectroscopy.....	77
5.9    Fluorescence Lifetime Imaging Microscopy .....	79
5.10    Summary and Future Research.....	80
APPENDIX A: DERIVATION OF EQUATION FOR NET FORCE ON EXCITON.....	83
APPENDIX B: REFLECTION AND ANGLE DEPENDENT INTENSITY.....	89
REFERENCES.....	93

## LIST OF TABLES

	Page
2.1 List of binary III-V nitrides, their bandgaps and their lattice constants .....	6
4.1 Material parameters used for calculating the excitonic wavefunction .....	41
4.2 Material parameters used to calculate the phonon dispersion relation .....	47
4.3 The PDPs and other parameters necessary to derive the strain dependent phonon dispersion relations.....	52
5.1 Decay constants and ratio of amplitudes of the radiative to nonradiative components of decay .....	68

## LIST OF FIGURES

	Page
2.1 Bandgap energies of the three main binary III-V nitrides and associated trinary compounds .....	5
2.2 Schematic diagram of ELOG-grown GaN.....	9
2.3 a, Schematic of the IHP QWs showing the variation in number of coupled QWs as a function of distance from the TD. b, Energy diagram showing the energy of the lowest level for the coupled QWs as a function of distance from the TD. c, The energy of the QW taking into account the built-in electric field which will be discussed in §2.4.1. d, Schematic of c-plane QWs falling into the IHP.....	10
2.4 TEM of an IHP showing the IHP QWs and their relation to the c-plane QWs (Hangleiter et al., Phys Rev Lett, 95, 127402 (2005)).....	11
2.5 a, Emission energy of the IHP and c-plane QWs as a function of temperature from 300 K down to 11 K. b, Decay lifetime of the IHP QWs and the c-plane QWs as a function of temperature .....	12
2.6 Typical band diagram for a single InGaN/GaN QW .....	14
3.1 Excitation in a direct (a), and indirect (b) bandgap semiconductor .....	19
3.2 Schematic diagram depicting the experimental setup used for PL .....	20
3.3 Schematic diagram of the temperature-dependent PL experiment.....	23
3.4 Schematic diagram of the angle-dependent PL experiment .....	24
3.5 Schematic diagram of the TRPL experiment .....	26
3.6 Schematic diagram of Near-field PL experiment .....	28
3.7 PL Spectrum from an InGaN/GaN multi-QW using the fitting model discussed in this section.....	31
4.1 a, Band-structure diagram of a single 2.5 nm $\text{In}_{0.20}\text{Ga}_{0.80}\text{N}/\text{GaN}$ QW .....	41
4.2 Schematic diagram of the structure used for the dispersion calculations .....	43
4.3 Plots of the dispersion relations for the upper and lower branches of the I-LO phonon modes for the heterostructure pictured in Fig 4.2 .....	46
4.4 Lower and upper branches of $\Gamma_m(q_{\perp}, z_{e,h})$ with the symmetric solutions in black and anti-symmetric in red with the associated mode number .....	50



4.5	The Huang-Rhys parameter $S$ as a function of the biaxial strain $\epsilon_{xx}$ in the system .....	52
4.6	Top-down images of the ELOG sample showing the ‘wing’ and ‘seed’ regions of the sample .....	53
4.7	a, Near-field topology of the sample showing the ‘wing’ and ‘seed’ regions. b, Near-field integrated photoluminescence intensity. c, The empirically derived Huang-Rhys parameter. d, The strain as derived using the inverse of the function $S(\epsilon_{xx})$ presented in Fig. 4.5 .....	56
4.8	Emission energy of common semiconductors versus their lattice constants .....	57
5.1	a, CW PL measurement of InGaN/GaN multi-QW system with embedded Au NPs (Red), Ag NPs (blue) and without NPs (black) at 77K (solid) and 300K (dashed). b, CW PL measurement for a similar structure with metal thin-films.....	60
5.2	Time-resolved PL measurement showing the decay lifetime of the reference (black), Au NP (red) and Ag NP (blue) samples .....	61
5.3	a, The carrier concentration as a function of distance from the Au NP in the steady-state model at temperatures from 11K to 300K .....	66
5.4	a, The carrier concentration as a function of time for the Au NP system. b, The same for the reference system .....	68
5.5	PL Intensity calculated using Eq. 5.4.5 for the Au NP (red) and reference (black) systems as a function of time after excitation by an instantaneous Gaussian pulse .....	69
5.7	Debye radius (nm) as a function of time and excitation power density for the reference system .....	70
5.6	PL Intensity as a function of incident power density for the Au (red circles) and reference (black squares) systems.....	70
5.8	a, Schematic diagram of the electron-hole pair and its image used for computing the net acceleration of the e-h pair. b, Net acceleration on an e-h pair with orientation $\theta$ and distance $d$ from the surface of the nanoparticle .....	72
5.9	a, The peak PL intensity as a function of the measurement angle $\theta$ for the reference (black), Au NP (red) and Ag NP (blue) samples. b, The integrated PL intensity as a function of the measurement angle.....	74
5.10	a, The Huang-Rhys parameter $S$ as a function of angle for the reference (black), Au NP (red) and Ag NP (blue) samples. b, The intensity of the main emission and first (dashed) and second (dotted) phonon replicas normalized with respect to the total emission (i.e. $I_{PR-0} + I_{PR-1} + I_{PR-2} = 1$ ) .....	75

5.11	a, Emission energy of the main emission for reference (black), Ag (blue) and Au (red) measured as a deviation from the reference emission energy of 2.984 eV. b, Emission energy of the first phonon-replica. c, Emission energy of the second phonon replica .....	76
5.12	a, Map of the integrated near-field PL intensity in a 1x1 micron region of the Au NP sample. b, Map of the PL intensity of the QWs within the pits in the same region .....	77
5.13	Huang-Rhys Parameter extracted via fitting the same 1x1 micron area depicted in Fig 5.12.....	78
5.14	FLIM imaging of a 10x10 micron region of the Au NP sample showing the (a) intensity and (b) decay constant of the sample.....	80
A.1	Schematic diagram of the exciton used for this derivation.....	84
B.1	Schematic diagram of the path of a light ray from a source outwards at three angles: $\theta$ , $\theta_c$ and $>\theta_c$ .....	90

## CHAPTER 1

### INTRODUCTION

#### 1.1 Semiconductors and Light Emission

As our understanding of semiconductors has advanced, semiconductors have come into use as sources for light emission. Semiconductor light emitters today are an important aspect of modern technology, providing everything from backlighting for modern LCD displays, head/tail-lights for cars, solid-state lasers for CD and DVD, solid-state laser pointers, LED flashlights and so on. More recently advances have been made towards using LEDs for solid-state indoor light sources [1, 2]. Due to the ubiquitous nature of semiconductor LEDs and laser diodes (LDs) much attention has been paid in recent years to the improvement of efficiency of semiconductor LED and LD systems. Originally much of the effort spent in improving efficiency of these devices was in optimization of growth techniques [3]. The quality of the heterostructures grown for light emission has a significant impact on the internal quantum efficiency (IQE) of the structure. Attention has also been paid to improving the external quantum efficiency (EQE) of the device by improving things like the light extraction efficiency using improved packaging methods [4].

#### 1.2 Plasmonics

One of the current avenues of investigation for improvement of device efficiency is through the modification of the IQE by resonant interaction of carriers within the light

emitter with surface plasmon polaritons (SPPs) present at a nearby metal-dielectric interface. These plasmons represent a collective excitation of electrons at the interface coupled to a photon. For a planar surface, the plasmons can freely propagate along the interface, and the electric field produced by the plasmon decays exponentially along the z-axis into both the dielectric and metal layers. For a metallic nanoparticle the plasmons are confined to the surface of nanoparticle and are known as localized surface plasmons (LSPs). For an LSP the electric field felt within the dielectric is dependent on the shape of the nanoparticle and whether the plasmon mode excited is a dipole or higher-order in nature. This evanescent field allows for interaction of the plasmon with carriers within the semiconductor.

When the SPP frequency is resonant to carriers within the semiconductor, coupling between the two significantly alters the recombination rate of carriers. This enhancement in the recombination rate is due to the Purcell effect [5]. Essentially it provides another recombination path resulting in a new recombination lifetime:

$$\frac{1}{\tau} = \frac{1}{\tau_{rad}} + \frac{1}{\tau_{nr}} + \frac{1}{\tau_{plasmon}} \quad (1.2.1)$$

Since  $\tau_{plasmon}$  is normally significantly lower than the radiative recombination lifetime  $\tau_{rad}$ , the overall recombination lifetime is reduced. This decrease in the lifetime results in an increase of radiative recombinations relative to the number non-radiative recombinations, and hence an increase in the IQE of the system.

Previous work using SPPs on InGaN/GaN multi-QW systems has shown that plasmonic coupling can produce a 10x enhancement in the photoluminescence (PL)

emission intensity of the system [6]. Similar results have also been obtained for other systems [7].

Despite early progress in showing PL enhancement under photo-excitation, much less progress has been made in harnessing plasmons for actual LED and LD applications. Specifically recent work has shown an enhancement of 1.5x in electroluminescence for an InGaN LED coupled to SPPs on silver nanoparticles embedded within the heterostructure [8].

Using SPP coupling to produce enhancement requires that the energy of the plasmons match that of the emission source. Unfortunately the plasmon energy is a function of the metal used and the geometry of the metal itself. The energy of SPPs is determined primarily by the metal used, and can be altered somewhat by the dielectric constant of the semiconductor and the dimensionality of the metal structure. In both cases the plasmon energy can only be lowered from the bulk energy. The lack of tunability and resonance requirement of plasmonics limits the range of energies over which it can be applied. This, combined with energy loss due to Joule heating at the metal-dielectric interface by the plasmons poses a challenge for plasmonics for light emission enhancement.

### 1.3 Non-resonant Enhancement and Strain Mapping

While plasmonics shows great promise for many applications, the requirement of resonant interaction and limitations in the plasmon frequencies of available metals limit its use for light emission enhancement. It is for this reason that I have pursued a non-resonant method of emission enhancement. Developing such a method would provide

enhancement over the entire spectrum without the need for tuning plasmon frequencies via alloying or limiting the emission frequencies to those which overlap with plasmon resonances.

In this work I provide a model for non-resonant light emission enhancement based on electrostatic interaction, as well as experimental evidence of the enhancement in an InGaN/GaN multiple quantum well (QW) system. The results of this research are presented in Chapter 5 of this work.

In the course of my investigation of this effect, I have also devised a means of extracting strain information from spectral data. This technique makes use of the phonon replicas which arise due to interaction of longitudinal optical (LO) phonons with carriers during recombination. I present here preliminary results of this technique used for strain mapping using a near-field scanning optical micro-spectrometer (NSOM) in Chapter 4 of this work.

## CHAPTER 2

### III-V NITRIDES

#### 2.1 Introduction to Nitrides

As far as semiconductor material systems go, the III-V nitrides are a fairly recent development. Major progress in the III-V nitrides was made in the '90s when gallium nitride (GaN) was successfully used to make blue LEDs and laser diodes (LDs). Despite the poor quality of the initial heterostructures, the strong demand for solid-state blue lasers and LEDs drove the development of GaN and InGaN/GaN heterostructures [9]. The development of solid-state white lighting using UV/Blue LEDs and a phosphorescent coating provided even more incentive to develop the nitrides.

Today the market for the nitrides has continues to expand. The blue lasers

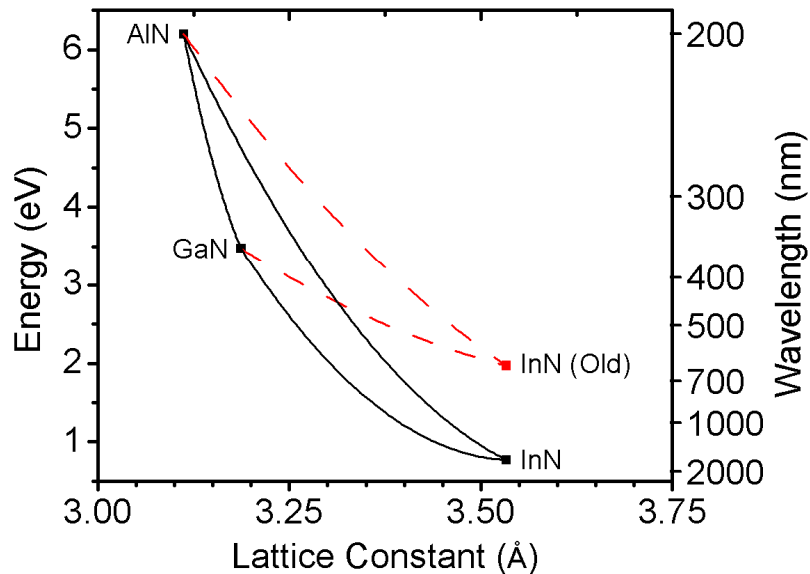


Figure 2.1 Bandgap Energies of the three main binary III-V nitrides and associated ternary compounds. The solid lines represent the bandgaps of the ternary compounds. The dashed red lines represent the estimated bandgaps based on the original estimate of InN's bandgap

derived from GaN heterostructures can be found in the nearly ubiquitous BluRay™ and DVD drives, as well as solid-state lighting and other uses such as laser pointers.

The primary nitride used is the aforementioned GaN. Generally GaN is used to as a substrate for other III-V nitride structures, as it is the easiest to grow directly on a substrate. The other binary nitride semiconductors that see use are aluminum nitride (AlN) and indium nitride (InN). Figure 2.1 shows the band-gap energy and lattice constants of the three binary III-V nitrides, along with the lattice constants and bandgap energies of their tertiary compounds.

Recent advancements in growing high quality InN films have allowed for more accurate measurements of the InN bandgap, which has led to the revision of the bandgap from 1.97 eV to 0.77 eV [10]. This change extends the range of possible energies achievable with the III-V nitrides all the way into the near infrared, including the optical fiber communication wavelengths 1330 nm and 1550 nm.

Table 2.1 List of binary III-V nitrides, their bandgaps and their lattice constants. All parameters from Reference [11] unless otherwise noted.

	$E_{\text{gap}}$ (eV)	$a$ (Å)	$c$ (Å)
GaN	3.47	3.187	5.186
AlN	6.2	3.112	4.982
InN	1.97 0.77 <sup>[10]</sup>	3.533	5.693



## 2.2 Tertiary Compounds and Heterostructures

In addition to the binary III-V nitrides, it is possible to grow ternary compounds such as AlGa<sub>x</sub>N and InGa<sub>1-x</sub>N. These compounds have the benefit of allowing for the tuning of the bandgap of the compound by adjusting the ratio of Ga:Al or Ga:In. The fractional composition of the tertiary compound is generally written as Al<sub>x</sub>Ga<sub>1-x</sub>N, where  $x$  is the Aluminum (or Indium) fraction of the alloy. The lattice constant of the alloy turns out to be simply related to the lattice constants of the two binary compounds the semiconductor is composed of. This relation is known as Vegard's law and it states that the lattice constant (or any other parameter which can be related in this way) for the alloy is given by [12]:

$$a_{AlGaN} = a_{AlN} x + a_{GaN} (1 - x) \quad (2.2.1)$$

Many other parameters, such as phonon frequencies [13] and piezoelectric constants [14], can be determined for alloys using Vegard's or a Vegard's-like law.

The bandgap, on the other hand, generally is not linear in the In or Al fraction used. Generally the dependence of the bandgap on the fraction  $x$  is given by a Vegard's-like relation with an additional bowing parameter  $b$  [11]:

$$E_g(Al_xGa_{1-x}N) = x E_g(AlN) + (1 - x) E_g(GaN) - b x (1 - x) \quad (2.2.2)$$

The solid and dashed lines in Figure 2.1 represent this relation for the ternary compounds derived from the binaries they connect, e.g. the line between AlN and GaN represents the bandgap of Al<sub>x</sub>Ga<sub>1-x</sub>N.

These compounds are generally not used in bulk structures, but are instead used in GaN heterostructures to provide either barriers for GaN quantum well in the case of AlGaIn, or as quantum wells confined by GaN barriers in the case of InGaIn. Progress has also been made on using them in quantum wire or quantum dot structures [15].

### 2.3 Growth Issues and Defects

Initial attempts at growing GaN and its alloys were limited to heteroepitaxial growth. This is due to the difficulty in producing high-quality GaN crystals for use as growth substrates [16]. Instead the initial substrate of choice was sapphire ( $\text{Al}_2\text{O}_3$ ). Although progress has been made on free-standing HPVE GaN substrates [16], most growth continues on sapphire or silicon carbide substrates.

Growth of the heterostructures can be done via molecular beam epitaxy (MBE) or metal-organic chemical vapor deposition (MOCVD). Until recently MOCVD resulted in higher quality samples and required less growth time than MBE [16]. This was part of the reason for the quick adoption of the nitrides for light emission, as MOCVD is fast enough to be used for commercial growth.

Due to the lattice mismatch between sapphire and GaN, a high number of defects occur at the interface between the two. The most common defect arising from this mismatch is the threading dislocation (TD), which can have dislocation densities between  $10^6$ - $10^{10} \text{ cm}^{-2}$ . Threading dislocations arise at GaN/sapphire interface at the boundaries of separate regions of GaN which are rotated with respect to each other oriented along the *c*-axis. These dislocations propagate to the surface from the substrate boundary, with some being annihilated or terminating before reaching the surface [16]. The efficiency of GaN and AlGaIn-based LDs and LEDs turns out to be

extremely sensitive to the threading dislocation density [3]. Therefore much effort has been made towards controlling the dislocation density in the GaN buffer sample. A number of techniques have been developed towards this end, many of which make use lateral growth to bend the threading dislocations, preventing them from reaching the surface of the buffer layer.

### 2.3.1 Epitaxial Layer Over-Growth

One such method is epitaxial layer over-growth (ELOG) [17]. In ELOG, a mask layer of  $\text{SiO}_2$  is grown atop a GaN seed layer and partly removed to provide apertures

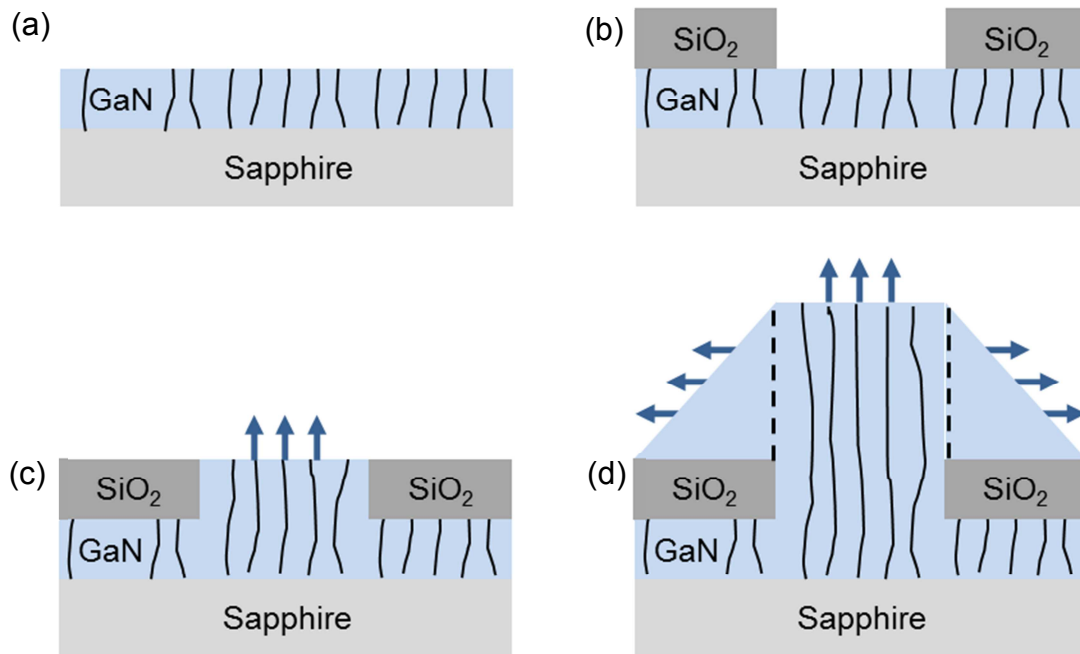


Figure 2.2 Schematic diagram of ELOG-grown GaN a, A GaN buffer is grown on sapphire substrate. b,  $\text{SiO}_2$  is grown on the GaN and partly removed to create a mask to constrain growth. c, Growth is resumed, and proceeds only through the apertures in the mask, the blue arrows signal the direction of growth. d, After the mask growth proceeds normal to the surface in the *seed* regions and parallel to the surface in the *wing* regions. TDs only remain in the seed region.

for continued growth of the GaN. The regions of exposed GaN are known as the “seed” regions, while those covered with  $\text{SiO}_2$  are referred to as the “wing” regions. When GaN growth is resumed, it begins normal to the surface in the seed regions. Once the GaN layer thickness is larger than that of the mask layer, the growth continues in two directions: Normal to the surface in the seed region, and parallel to the surface in the wing region. Figure 2.2 contains a schematic diagram of the growth of a GaN buffer using ELOG. The end result of this growth is a wing region almost entirely devoid of TDs.

### 2.3.2 Inverted Hexagonal Pits and TDs

While AlGaIn and GaN heterostructures are sensitive to TDs, it turns out that InGaIn heterostructures seem to be insensitive to their presence [18]. This is due to the

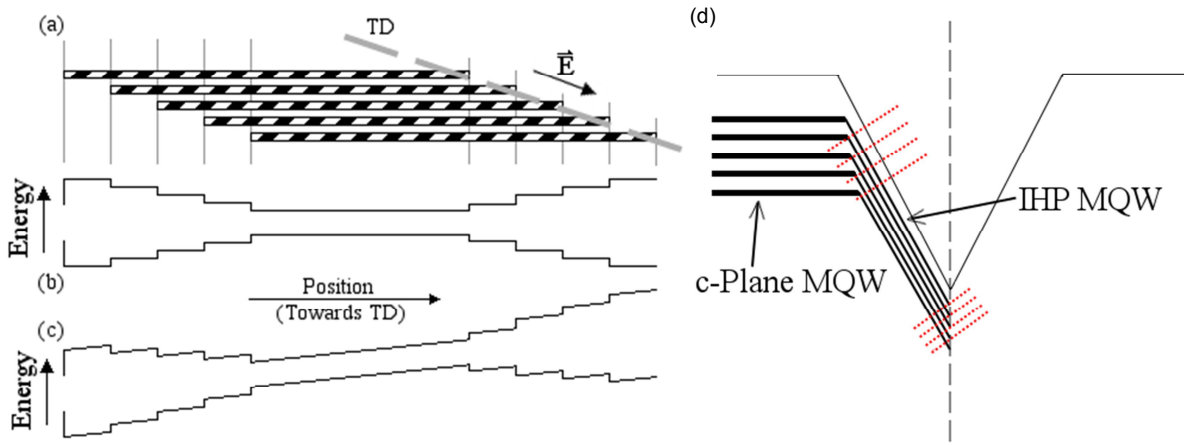


Figure 2.3 a, Schematic of the IHP QWs showing the variation in number of coupled QWs as a function of distance from the TD. b, Energy diagram showing the energy of the lowest level for the coupled QWs as a function of distance from the TD. c, The energy of the QW taking into account the built-in electric field which will be discussed in §2.4.1. d, Schematic of c-plane QWs falling into the IHP. Area between the red lines corresponds to a.

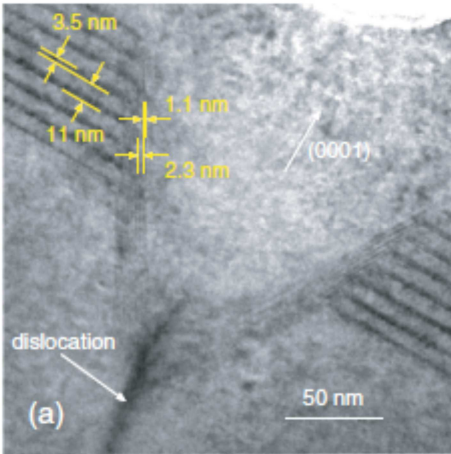


Figure 2.4 TEM of an IHP showing the IHP QWs and their relation to the *c*-plane QWs. (Image from Hangleiter et al., *Phys Rev Lett*, **95**, 127402 (2005)).

formation of inverted hexagonal pits (IHPs) at the TDs during the growth of InGaN layers atop a GaN buffer. These pits are crystallographic defects which are centered upon the TD and are constrained by the  $\{10\bar{1}1\}$  facets of the crystal [19]. During growth of InGaN MQW structures it has been shown that the QWs bend at the IHP boundary and grow down into the IHP along the  $\{10\bar{1}1\}$  facets. These IHP QWs are narrowed with respect to the main QW structure, e.g. a 2.5 nm QW narrows to  $\sim 1.1$  nm

within the IHP. Hangleiter, et al. showed that this narrowing of the quantum well provides a potential barrier that shields the carriers in the main QW from the TD [20]. Figure 2.3d depicts the structure of an IHP with the main QW falling into the IHP. Figure 2.4 presents TEM of the same structure as imaged by Hangleiter, et al. [20]

More recently, my work has shown that the potential within the IHP QWs is further complicated by coupling between the wells which leads to a step potential within the IHP multi-QW structure [21]. This coupling arises due to the fact that the barrier between the IHP QWs is significantly narrowed compared to the width IHP QWs. In the previously mentioned work by Hangleiter, it is shown that while the 3.5 nm QW is reduced to  $\sim 1$  nm, the 7.5 nm barrier is also reduced to  $\sim 1$  nm. This creates a coupled QW system where the number of energy levels is related to the total number of coupled QWs. A schematic of a 5 QW system within the IHP and the lowest energy level as a function of position within the wells is presented in Figure 2.3b. Note that each QW

within the IHP is offset slightly, leading to regions with differing numbers of coupled QWs. It is well known that the splitting resulting from coupled QWs results in a decrease in the energy of the lowest energy state within the QW as the number of coupled QWs increases. This gives rise to the stepped energy structure depicted in the schematic.

One consequence of this structure is a sharp red-shift in the energy of IHP QW emission at low temperature when the degeneracy of the step states is lifted. That is, above a certain temperature the thermal energy is larger than the difference between the adjacent energy levels, thus rendering the states degenerate. When the temperature drops below this level, new states become available, and the carriers are able to relax into lower energy states, resulting in a red-shift emission energy with temperature instead of the expected blue-shift. Figure 2.5a shows the energy of emission of the IHP QWs as compared to the c-plane QWs. Note that the energy of emission of the c-plane QWs continues to increase as temperature decreases. The IHP

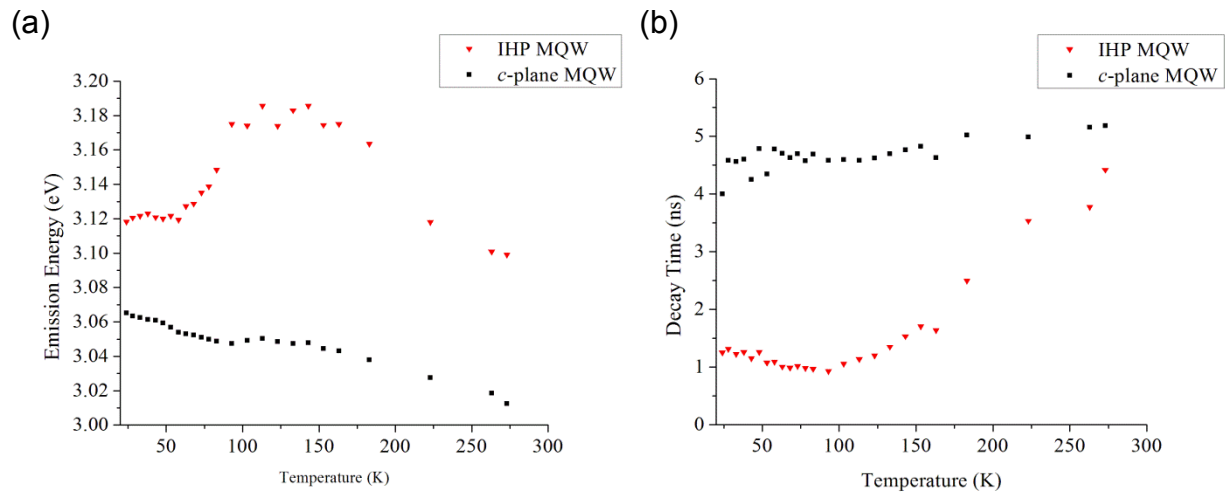


Figure 2.5 a, Emission energy of the IHP and c-plane QWs as a function of temperature from 300 K down to 11 K. b, Decay lifetime of the IHP QWs and the c-plane QWs as a function of temperature.

QWs, on the other hand, show an increase in emission energy only up down to 100K, after which there is a sharp decrease in emission energy until the energy levels out at ~50K.

In addition to the anomalous energy shift, there is evidence of this structure in the decay lifetime of the IHP QW emission. Figure 2.5b shows the lifetime of the IHP QWs as compared to that of the *c*-plane QWs. The most important feature to note here is the minimum in the lifetime that corresponds with the transition temperature of 100K. Above this temperature the carriers in the IHP QW are unaffected by the energy level structure of the QW and are free to move within the IHP. Due to the built-in electric field of the QW which is oriented along the *c*-axis of the QW, there is an in-plane electric field experienced by the carriers, as shown in the skewed energy diagram in Figure 2.3c. This field acts to separate the carriers, reducing the overlap in the electron and hole wavefunctions, thus decreasing the recombination rate and increasing the lifetime. Additional thermal energy acts to weaken the excitonic bonding, resulting in larger separations and lifetimes.

Below the transition temperature, the step structure begins to affect the carriers. The carriers relax into the lowest energy section of the IHP QW, which shields them from recombining non-radiatively at the TD. Lower temperatures result in better shielding and hence a lower probability of non-radiative recombination. Generally the non-radiative recombination lifetime is quick compared to the radiative lifetime, so reducing the probability of non-radiative recombination results in the increase in lifetime observed for temperatures below 100K.

## 2.4 Piezoelectricity and the Quantum-Confined Stark Effect

In addition to the aforementioned IHPs which arise in InGaN/GaN heterostructures, there are a couple of interesting features which are observed in these systems. The first feature I will discuss is the built-in electric field which arises in InGaN/GaN heterostructures due to spontaneous polarization at the GaN/InGaN interfaces [14] and the piezoelectric nature of InGaN [22]. The electric field that is produced is a function of the strain in the system, quantum well width and the indium fraction used, and runs parallel to the  $c$ -axis of the heterostructure [23].

The piezoelectric polarization is given by the equation:

$$P_z = e_{31}\epsilon_{xx} + e_{31}\epsilon_{yy} + e_{33}\epsilon_{zz} \quad (2.4.1)$$

where  $e_{31}$  and  $e_{33}$  are components of the piezoelectric tensor for InGaN, and  $\epsilon_{xx,yy,zz}$  are

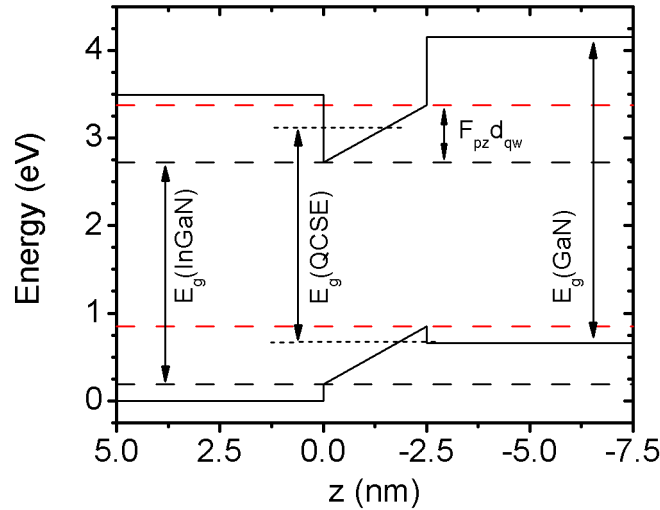


Figure 2.6 Typical band diagram for a single InGaN/GaN QW. The band bending due to the internal electric field results in a separation of the electron and hole and a reduction in the bandgap energy.



the strains in the  $x$ ,  $y$  and  $z$  directions ( $z$  being parallel to the  $c$ -axis). Assuming biaxial strain and pseudomorphic growth, we can assume that  $\varepsilon_{yy} = \varepsilon_{xx}$  and that  $\varepsilon_{zz} = -2(c_{13}/c_{33}) \varepsilon_{xx}$ , where  $c_{13}$  and  $c_{33}$  are stiffness constants. This gives us:

$$P_z = 2 [e_{31} - (c_{13}/c_{33})] \varepsilon_{xx} \quad (2.4.2)$$

This can be converted into an electric field simply by dividing by  $\epsilon_r \epsilon_0$ .

The presence of this electric field within the QW leads to a separation of the carriers to opposite ends of the QW, leading to a reduction in overlap of the electron and hole wavefunctions. This reduced overlap causes an increase in the radiative recombination lifetime of the QW. Furthermore, the skewing of the band structure due to the electric field effectively reduces the energy separation between the electron and hole states, resulting in a red-shifted emission. Figure 2.6 shows a typical band-structure of an InGaN/GaN QW structure. This red-shift due to the built-in electric field is known commonly as the quantum-confined Stark effect (QCSE) [22].

The strength of the QCSE turns out to be excitation-power-dependent. As carriers are excited, they separate out to opposite sides of the QW and thereby screen some of the electric field. At high excitation-power densities, the number of carriers becomes large enough to effectively screen the internal electric field, resulting in a blue-shift in emission and a decrease in the recombination lifetime [24]. Furthermore QCSE has been shown to produce non-exponential decay in InGaN QWs due to the dependence of the lifetime on the carrier concentration, and hence on time. [25]

## 2.5 Electron-Phonon Interactions and Phonon Replicas

The second interesting feature of InGaN/GaN QWs is strong electron-phonon coupling. This coupling arises due to the carrier separation caused by the built-in electric field, which induces to a polarization of the lattice around the carriers. This polarization allows the lattice to interact with the carriers directly, resulting in enhanced electron-phonon interactions.

There are three primary modes of electron-phonon interaction in InGaN: Piezoelectric interaction by carriers with acoustic phonons, deformation potential interaction with acoustic and optical phonons, and Fröhlich interaction with longitudinal optical (LO) phonons. Of these three we are primarily interested in the Fröhlich interaction. The interaction between an electron-hole pair and an LO phonon is described by the Hamiltonian [26]:

$$H_{ex-ph} = \sum_{n,n',k,q} V^{nn'}(\mathbf{q}) B_{n,k+q}^\dagger B_{n,k} (a_q + a_{-q}^\dagger) \quad (2.5.1)$$

Here  $B$  and  $a$  are the exciton and phonon construction and destruction operators respectively,  $V^{nn'}(\mathbf{q})$  is the exciton-phonon interaction matrix element,  $q$  the phonon wavevector,  $n$  the initial electronic state, and  $n'$  the final electronic state.  $V^{nn'}(\mathbf{q})$  takes the form [26]:

$$V^{nn'}(\mathbf{q}) = \int d^3\mathbf{r} \psi_n^*(\mathbf{r}) \psi_{n'}(\mathbf{r}) \left[ F_q^e e^{-i\frac{m_e}{M}\mathbf{q}\cdot\mathbf{r}} - F_q^h e^{-i\frac{m_h}{M}\mathbf{q}\cdot\mathbf{r}} \right] \quad (2.5.2)$$

where  $F_q$  is the electron-LO or hole-LO coupling constant for Fröhlich interaction.

One of the primary results of this interaction is the production of LO phonon replicas (PRs) in the PL emission spectrum. A PR is a secondary peak offset from the main emission of the QW by the energy of one or more LO phonons. They arise due to the emission or absorption of one or more LO phonons upon radiative recombination. Since the phonon replicas depend on the energy and wavevector of the LO phonons involved [26], they carry information about strain in the system, as the phonon energy is dependent on the strain in the system [27]. This feature can be made use of to allow us to extract strain information from the QW's spectrum.

## CHAPTER 3

### EXPERIMENTAL METHODS

#### 3.1 Introduction

In investigating the aforementioned material system, I will make use of several well-known experimental techniques in order to quantify aspects of the III-V nitride samples I have obtained. In this case, I am interested primarily in the light-emission or luminescence characteristics of the sample. There exist many techniques for producing luminescence within a light-emitting semiconductor including electroluminescence (excitation by driving a current through the system), cathodoluminescence (excitation by injecting electrons directly into the sample), and photoluminescence (excitation by an incident light-source such as a laser). I will focus primarily on photoluminescence (PL) techniques in this chapter, and how to interpret/analyze the spectral data that is the result of the measurements.

#### 3.2 Origin of Luminescence

Before I continue, it is helpful to have a brief refresher on the mechanisms which result in light-emission from a semiconductor. In a semiconductor, there exist two sets of energy levels known collectively as the valence and conduction bands. These bands arise due to the creation of forbidden energy gaps in the motion of an electron within a periodic potential like the lattice of a semiconductor [28].

The separation in energy between the highest occupied energy level in the valence band and the lowest unoccupied energy level in the semiconductor is known as

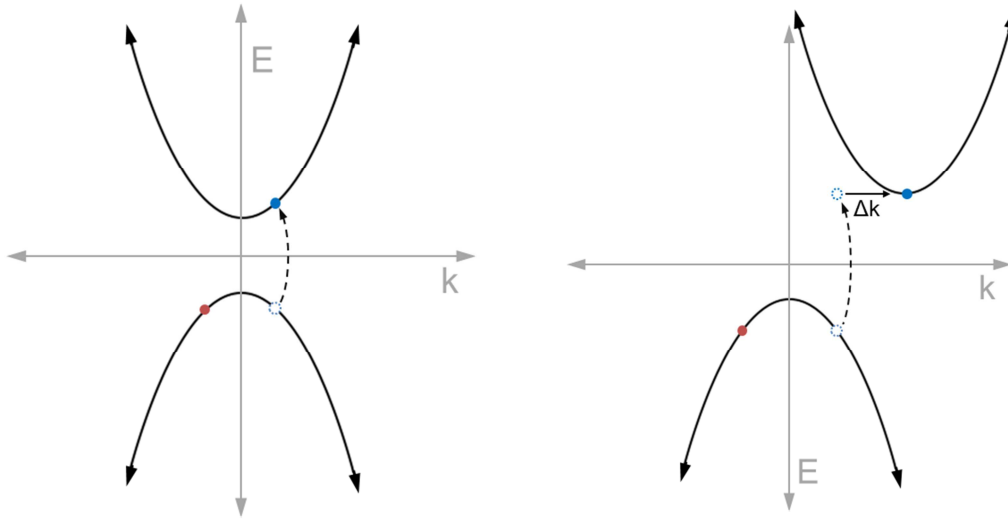


Figure 3.1 Excitation in a direct (a), and indirect (b) bandgap semiconductor. The upper parabola represents the conduction band and the lower parabola represents the valence band. The final result of excitation in both cases is an electron (blue circle) in the conduction band and a hole (red circle) in the valence band. In the indirect case, emission or absorption of a phonon with wavevector  $\Delta k$  is required to complete the excitation.

the bandgap. This energy is the minimum energy required for a carrier to be excited from the valence to the conduction band. If we were to provide an electron in the valence band with this amount of energy, we are left with the excited electron in the conduction band, and an absence of an electron, known as a hole, in the valence band. Eventually, in the simplest case, the electron will recombine with the hole freeing up an amount of energy equal to the bandgap energy. If the semiconductor is a “direct gap” semiconductor, then the momentum of the excited electron and hole match up, and recombination can occur via the production of a photon. In the case of an “indirect gap” semiconductor, momentum conservation cannot be fulfilled solely by emission of a photon, and so the difference in momentum must be compensated for by emission of one or more phonons (quanta of vibrations in the lattice).

### 3.3 Far-field vs. Near-field

It is possible to divide PL measurements into two regimes, measurements in the far-field, and measurements in the near-field. Far-field measurements are the most common form of PL, and result from the measurement of the optical far-field, i.e. the photon that is produced upon carrier recombination. Because of this, far-field measurements are subject to the diffraction limit for the maximum resolution achievable. The majority of experimental methods used in this work are far-field measurements.

Near-field measurements, on the other hand, involve interaction with the evanescent fields near the emitter. This evanescent field decays exponentially with distance from the emitter, and is not subject to the diffraction limit. Later in this chapter I

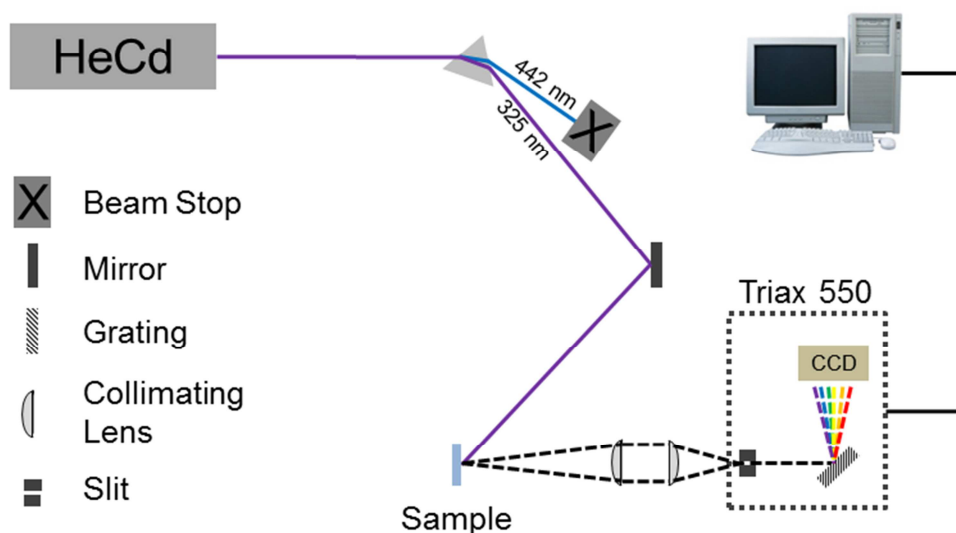


Figure 3.2 Schematic diagram depicting the experimental setup used for PL. Excitation from the HeCd CW laser proceeds through a prism to split out the 442 nm beam line, then the remaining 325 nm line is directed to the sample. Photoemission from the sample is collected and focused on the entry slit of a Triax 550 spectrometer using a pair of collimating lenses. The CCD output is then sent to the computer and transformed into spectral data.

will cover near-field measurements using a near-field scanning optical micro-spectrometer (NSOM).

### 3.4 Far-field PL

The most common method of characterizing a light-emitting sample is through far-field PL measurements. In this experiment the sample is excited—in this case an InGaN/GaN MQW—and the wavelengths of the emitted photons are measured. Generally this measurement is achieved using either a monochromator (which uses a diffraction grating to single out a very narrow range of wavelengths) along with a photodiode to measure the intensity at that wavelength, or a diffraction grating combined with a CCD (charge-couple device) detector. The latter has the benefit of being able to simultaneously capture the intensities over a wide range of wavelengths, speeding up the process significantly.

Figure 3.2 depicts the experimental setup used for PL measurements in this work. Excitation is achieved using the 325 nm line of a HeCd continuous-wave (CW) laser. The 442 nm line of the HeCd is separated out using a prism and beam stop, and the remaining line is directed to the sample using UV-Vis mirrors. The emission from the excited sample is then directed through a pair of collimating lenses to focus the emitted light on the entry-slit of a Triax 550 spectrometer, which contains the aforementioned diffraction grating and CCD.

The result of the measurement is a spectrum which displays the emitted intensity versus wavelength (or energy) of the photons. It is important to note that this measured intensity depends directly upon many factors, e.g. the alignment of the laser and

sample, alignment of the collimating lenses, slit-width, time of integration of the CCD, etc. Because of this, great care must be taken when directly comparing measured intensities between samples. Furthermore, it is for this reason that the units of measured intensity in PL measurements are generally labeled a.u. or arb, short for arbitrary units.

Even in the absence of direct comparisons of intensities between spectra there is still a significant amount of information that can be extracted from spectra. For instance, if we normalize the spectra such that the total area under the curve is unity, then the intensity represents the probability of emission at that wavelength. In many cases the distribution of probabilities is or is close to Gaussian, and so we can estimate not only the peak energy of emission but also other parameters such as the full-width at half-maximum (FWHM) which is related to the standard deviation of the energy of the photons, and identify other emission peaks as well. I will discuss how to extract this information in detail at the end of this chapter.

While a spectrum taken at room temperature gives us a good deal of information about the sample, we can gain more information if we tweak one variable while holding the others constant. The next three sections involve variations of PL using this method.

#### 3.4.1 Temperature Dependent PL

Temperature in a semiconductor affects many properties of the sample. For example the concentration of phonons within the medium decreases with decreasing temperature, as does the mobility and average velocity of excited carriers within the system. Additionally, the probability of non-radiative recombination with defect sites



decreases at lower temperatures, resulting in an overall increase in the quantum efficiency of the system.

In order to vary the temperature of the sample for measurement the sample is placed within a cryostat with a viewing port such that the excitation source (laser) can enter through the window, and the emitted light can be collected out the same window. The cryostat is controlled by a temperature controller and allows for the temperature to be varied between 11 and 300 K. The sample is allowed to come into thermal equilibrium with the cryostat after each temperature change over 30 minutes. Figure 3.3 depicts the experimental setup used for temperature-dependent PL measurements.

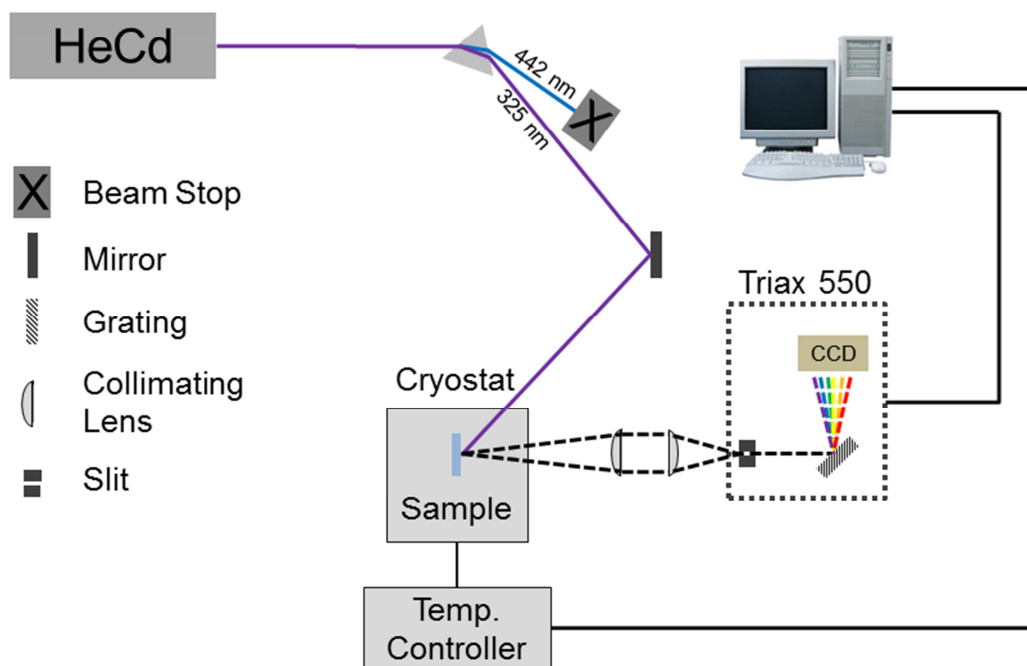


Figure 3.3 Schematic diagram of the temperature-dependent PL experiment. The primary change is the insertion of the sample into a cryostat, which is used to vary the temperature of the sample from room temperature (300 K) down to around 10 K. The experiment is repeated at multiple temperatures, and the spectrum at each temperature recorded to provide a description of the change in emission with temperature.

### 3.4.2 Angle-Dependent PL

For angle-dependent PL measurements there are two possibilities for measure. Either the emitted PL spectrum is measured as a function of the angle of incidence of the excitation source, or as a function of the angle of emission from the sample. The former should contain some information about the absorption properties of the sample as a function of the incident angle, whereas the latter should carry more information about the recombination processes within the system.

In this experiment case I have measured the spectrum as a function of emission angle since the electron-phonon coupling resulting in phonon replicas is strongly wavevector dependent [29]. In order to make the measurements, I mounted a fiber optical waveguide on an arm attached to a goniometer base centered beneath the

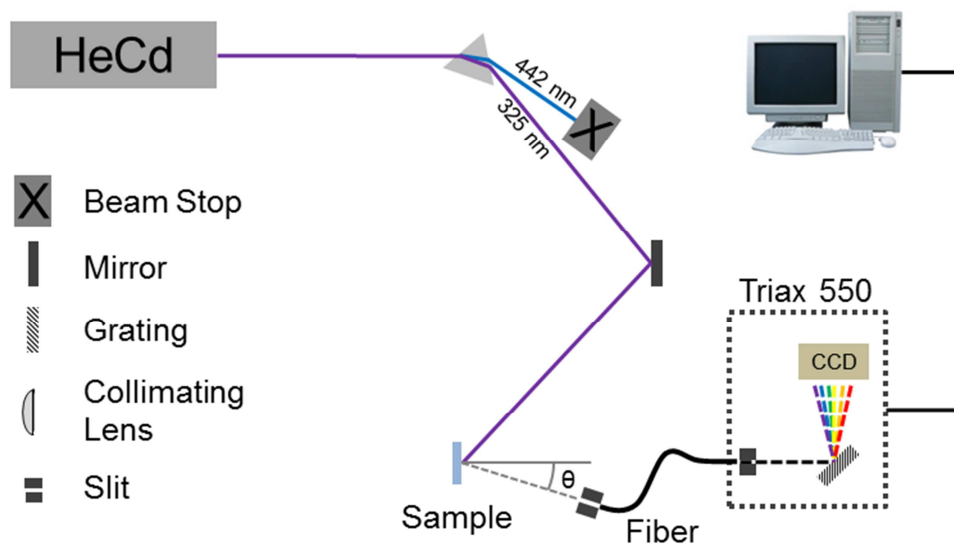


Figure 3.4 Schematic diagram of the angle-dependent PL experiment. A fiber optical waveguide is mounted along with an iris on a goniometer-mounted arm centered on the sample. The angle of rotation is measured relative to the normal of the sample. The fiber then connects directly to the Triax spectrometer using a fiber mount adapter.

sample. This allowed the arm, and hence the fiber, to rotate freely with the sample as the center of rotation. Due to the grading of the goniometer, the measurements were taken every  $5^\circ$  from  $-15^\circ$  from normal to  $90^\circ$ . Measurement of the full range of measurements ( $-90^\circ$  to  $90^\circ$ ) was not possible due to the position of the incident beam and the length of the fiber.

Excitation was achieved as with the other PL experiments, with the angle of incidence of the laser determined to be  $-55^\circ$  relative to normal. The reflected portion of the laser signal at  $55^\circ$  was filtered out using a 325 nm line filter, and additional background due to fluorescence of the fiber was subtracted out from the final spectra using a reference glass sample. Figure 3.4 depicts the experimental layout used.

### 3.5 Time-resolved PL

Time-resolved PL measurements (TRPL) differ from normal PL measurements in terms of both the excitation source and the detector used. In order to measure the time-dependent emission of the sample, we first need a time-varying source. Were we to use a CW excitation, we would only be able to measure a time-dependence during the transient phase when the excitation source was turned on initially. After a short ( $< 10$  ns) period, the system would reach equilibrium and thereafter there would be no time-dependence to measure. Therefore this experiment uses a pulsed excitation source instead of a CW source in order to excite the sample. It is important to note that the frequency of the excitation (and duration of the pulse) plays a large role in determining the sorts of interactions which can be studied using TRPL. Specifically, the frequency should be slow enough that the system returns to the ground state after each pulse, and

the duration of the initial pulse should be significantly shorter than the timescales of the interactions being observed. For a typical semiconductor, the majority of carrier dynamics fall within a timescale between 1 ps (e-e/e-h/e-ph scattering) and 10 ns (e-h recombination) [30]. To study these interactions I used a Mai-Tai Ti:Sapphire Femtosecond laser with a repetition frequency of 80 MHz, which equates to 12.5 ns between pulses. The laser's fundamental was set to 750 nm and passed through a doubler to give an excitation wavelength of 325 nm. Power was kept at 10 mW for the temperature dependent TRPL measurements. The experimental setup for TRPL is depicted in Figure 3.5.

### 3.5.1 Power-Dependent TRPL

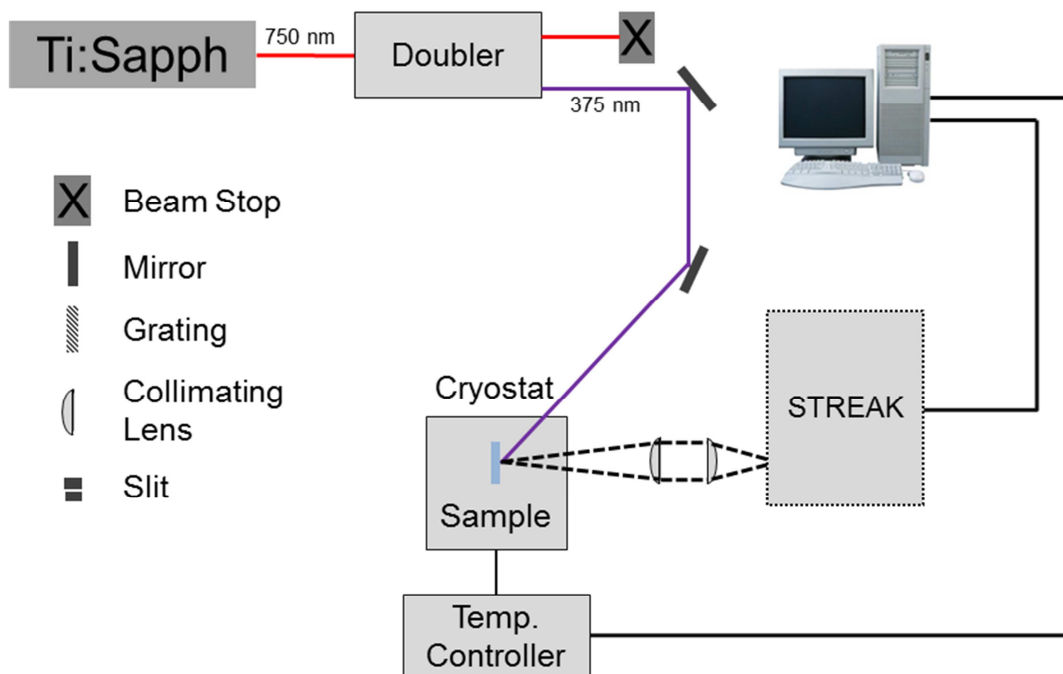


Figure 3.5 Schematic diagram of the TRPL experiment. Excitation via a Ti:Sapphire pulsed laser run through a doubler to produce a 375 nm excitation wavelength. Emission from the sample is collected and collimated using a pair of collimating lenses and then fed into the entry slit of a STREAK camera to measure the time-dependence of the emission.

Power-dependent PL simply entails using a neutral density filter mounted after the doubler in Fig 3.5 to control the intensity of the laser incident on the sample. A power meter was used to measure the incident power down to the nearest 0.1 mW. In our experiments I varied the power between 1 and 100 mW.

### 3.6 Near-field PL

Near-field PL measurements involve measurements of the optical near-field using either a fiber probe or a metal-coated AFM tip. The goal is to produce an optical near-field at the end of the probe which can then interact directly with the sample. This near-field is the evanescent field resulting from the interaction of photons with the metal-coated AFM tip, or a sub-wavelength aperture in a metal-coated fiber probe. Due to the nature of the optical near-field, there is no diffraction limit to the resolution of the measurement, allowing sub-wavelength variations in emission properties of the sample to be studied.

There are three possible “modes” of near-field measurement: illumination, collection and illumination/collection. These refer to whether the excitation of the sample and/or the measured spectrum is produced via near-field interaction with the sample. Illumination mode involves excitation of the sample via a near-field source, and then measurement of the resultant far-field emission from the sample. Collection involves collection via near-field interaction of the emission resulting from excitation of the sample using far-field illumination. Illumination/collection mode, then, involves both illumination and collection in the near-field. Fiber-probe-based NSOM is capable of all three modes of operation, but suffers in topographical resolution due to the size of the

tapered fiber probe tip used for measurement. AFM-style probes, on the other hand can have AFM-quality topography, but generally sacrifice the ability to collect in the near-field. It is possible to bypass this by having an aperture in the AFM probe tip, however this generally increases the size of the probe and therefore reduces the topographical resolution.

For our near-field measurements I made use of a commercial JASCO NFS-330 near-field scanning optical micro-spectrometer (NSOM) using a tapered fiber probe operating in illumination/collection mode. Fiber probe aperture diameters used varied

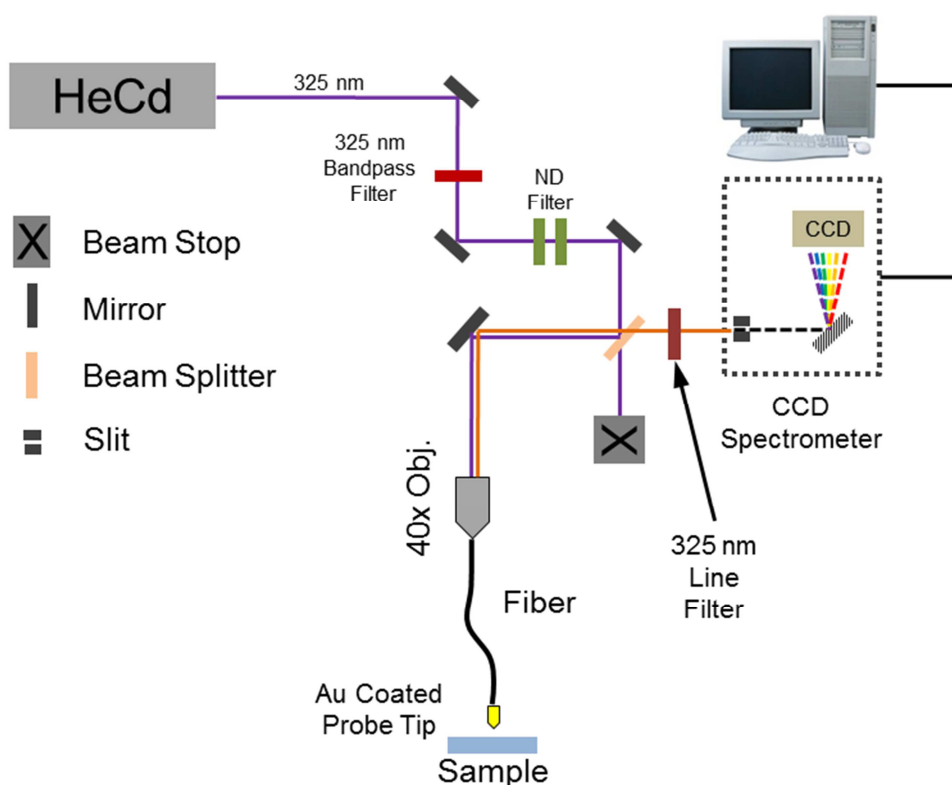


Figure 3.6 Schematic diagram of Near-field PL experiment. Excitation provided by the 325 nm line of a HeCd laser is passed through a series of filters to control the strength and then coupled into a UV fiber to couple the excitation via to the sample via near-field interactions. The sample returns emission via near-field interaction with the probe tip back through the fiber, through a line filter to eliminate the laser line and to the spectrometer.

between 120 and 300nm. Excitation was provided by the 325 nm line of the same HeCd laser used for far-field PL measurements, fed into the fiber through a UV-vis 40x objective. The spectral data was recorded using the NSOM's built-in CCD-based spectrometer.

### 3.7 Fitting Spectra

Most spectra will consist of one or more peaks of Gaussian or Lorentzian shape. These peaks are generally produced by different phenomena, such as the phonon replicas mentioned in the previous chapter. By fitting the data with a series of Gaussians it is possible to extract information about these peaks which can then provide further insight into the phenomena being studied. Even for a simple spectrum consisting of a single Gaussian fitting the result can help to extract parameters such as the center of emission and the full-width at half-maximum (FWHM) which might otherwise be obscured by noise.

While there are significant advantages to fitting spectral data, there are also serious pitfalls involved. The simplest way to make the dangers of fitting clear is to remember that *any* curve can be approximated by a sufficient number of Gaussians. Therefore it is important to have a model for the emission which is based on the underlying physics. This model should include an understanding of the number of emission peaks, the relations between them, and reasonable starting guesses for their energy, FWHM and amplitude. Furthermore the model should place constraints on the parameters to ensure that the peaks cannot swap positions from measurement to measurement.

In this work I have developed model for fitting the emission from the InGaN/GaN QWs mentioned in the previous chapter based on previous works which used fitting in a similar system [31]. The model uses a main peak with two phonon replicas to represent the emission of the main QW, and an independent high-energy peak to represent the emission of the IHP QWs. Each peak is represented by a single Gaussian:

$$I_j(\varepsilon) = A_j e^{-\left(\frac{\varepsilon - \varepsilon_j}{\delta_j}\right)^2} \quad (3.7.1)$$

Here  $A_j$  is the amplitude,  $\varepsilon_j$  the center in energy, and  $\delta_j$  the FWHM of the Gaussian. The full equation would then be

$$I(\varepsilon) = \sum_{j=1}^4 I_j(\varepsilon) \quad (3.7.2)$$

where we take  $j=1$  to represent the IHP peak,  $j=2$  the main QW peak and  $j=3,4$  to be the first and second phonon replicas respectively. Next we note that for a system with phonon replicas we can assume that the FWHM of the peaks should be equal [31], so we can set  $\delta_2 = \delta_3 = \delta_4$ . The FWHM of the IHP QW peak must remain independent due to the difference in the QW thickness and the presence of a threading dislocation, which acts as a non-radiative recombination center, at the center of the IHP [32, 33].



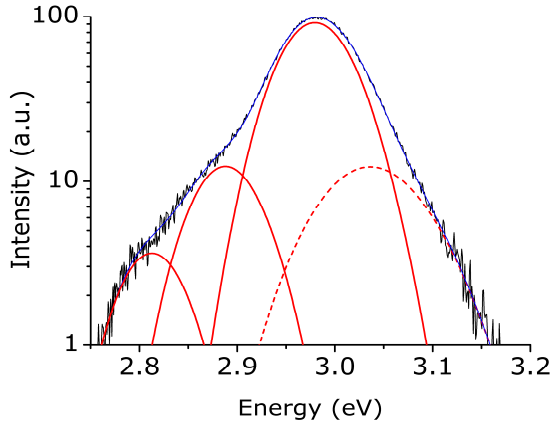


Figure 3.7 PL Spectrum from an InGaN/GaN multi-QW using the fitting model discussed in this section. The three solid Gaussians represent (from right to left) the main QW peak and the two phonon replicas. The dashed red line represents the IHP QW peak.

The energy of a phonon replica should be separated from the energy of the main peak by an amount equal to  $n \hbar \omega_{LO}$  [31]. Furthermore we know that the center of the phonon replica is actually displaced from this value by an amount equal to  $3/2 kT$  for the first phonon replica and  $1/2 kT$  for the second phonon replica [29, 34]. We therefore use the following relation to

provide an initial estimate of the positions of the two replicas:

$$\begin{aligned} \varepsilon_3 &= \varepsilon_2 - \hbar \omega_{LO} + \frac{3}{2} kT \\ \varepsilon_4 &= \varepsilon_2 - 2 \hbar \omega_{LO} + \frac{1}{2} kT \end{aligned} \tag{3.7.3}$$

We also add the constraint that the energy of the two peaks can vary from the initial energy by no more than  $\pm 3/2 kT$  for the first replica and  $\pm 1/2 kT$  for the second.

The only thing left is to provide accurate starting guesses for the IHP peak and the main peak of the QW. Due to the nature of the IHP QWs, we can assume that there is some relation between the energy of the main QW and the IHP QW [32]. Therefore it is sensible to make an initial guess for the energy IHP QW that is relative to the main QW emission:

$$\varepsilon_1 = \varepsilon_2 + \delta\varepsilon_{IHP} \quad (3.7.4)$$

For our system I have found  $\delta\varepsilon_{IHP} \approx 130 \text{ meV}$  makes for a good starting guess, and allow the energy to vary +/- half that value. Figure 3.7 depicts a fit using this model of a typical spectrum from our system.

### 3.8 Fitting TRPL Decay Measurements

Another important use of fitting is in determination of the radiative and non-radiative recombination lifetimes from the decay of the measured intensity with time in TRPL experiments. The most general and most commonly used model for fitting is that of an exponential decay. That is to say that the intensity can be modeled as following the following equation:

$$I(t) = A e^{-t/\tau} \quad (3.8.1)$$

where A is some amplitude, t is the time, and  $\tau$  is the decay constant, i.e. the time over which  $1/e \approx 36\%$  of the original intensity of the signal remains. This definition of the decay constant is analogous to the lifetime of carriers undergoing recombination obeying the rate equation:

$$\frac{\partial n}{\partial t} = \tau^{-1} n \quad (3.8.2)$$

Here n is the carrier concentration, and  $\tau$  is known as the radiative recombination lifetime, or just recombination lifetime in the absence of other forms of recombination.

The experimentally measured decay constant and the recombination lifetime can be considered to be proportional only when recombination within the light-emitting structure is essentially homogeneous and not subject to any electric fields in directions lacking quantum confinement. This requirement arises from the fact that the experimentally measured quantity, the intensity per unit time, is defined to be:

$$I(t) = \iint_{\mathcal{A}} \tau^{-1} n(\mathbf{r}, t) d\mathbf{r} \quad (3.8.3)$$

If the carrier concentration is homogenous over the area being measured, and there are no electric fields, then  $n$  is independent of position, and the integral above evaluates simply to  $\mathcal{A} \tau^{-1} n$ , where  $\mathcal{A}$  is the area of the region of measurement. Therefore the decay constant  $\tau_{decay}$  for the intensity in this situation would be given by:

$$\begin{aligned} \frac{\partial I}{\partial t} &= \tau_{decay}^{-1} I \\ \tau_{decay}^{-1} &= I^{-1} \frac{\partial I}{\partial t} \\ &= I^{-1} \frac{\partial}{\partial t} \iint_0^{\mathcal{A}} \tau^{-1} n d\mathbf{r} = I^{-1} \iint_0^{\mathcal{A}} \tau^{-1} \frac{\partial n}{\partial t} d\mathbf{r} \\ &= I^{-1} \tau^{-1} \iint_0^{\mathcal{A}} \tau^{-1} n d\mathbf{r} = I^{-1} \tau^{-1} I \\ \tau_{decay}^{-1} &= \tau^{-1} \end{aligned} \quad (3.8.3)$$

Hence the two are equal.

Carriers generally only obey this rate equation when there is a minority carrier within the QW. In this case the minority carrier concentration determines the recombination rate and we can treat recombination as proportional to the minority concentration. In cases where there is no minority carrier, we must treat recombination as being proportional to  $n \cdot p$ , the concentration of electrons times the concentration of holes. If the system is homogeneously excited, then we can assume that  $n \approx p$  and that recombination proceeds as:

$$\frac{\partial n}{\partial t} = -B n^2 \quad (3.8.2)$$

Where  $B$  is proportional to the probability of recombination, and the recombination lifetime is defined to be the concentration dependent value  $1/Bn$ . It is still the case, however that the decay constant is proportional to the recombination lifetime.

In cases where the two are not proportional, as in our system in Chapter 5, the decay constant still provides information about the time-dependent behavior of the system, and can be quite useful. Great care, however, must be taken to avoid using the decay constant in this case to draw direct conclusions about the recombination rate.

## CHAPTER 4

### SPECTRAL STRAIN MAPPING

#### 4.1 Introduction

In semiconductor nanostructures, defects can strongly affect the structure's efficiency. Defects result in local changes to the lattice, thereby affecting the local strain. Local strain measurements, therefore, provide a means of assessing the quality of semiconductor nanostructures. Advancements in high-resolution X-ray diffraction [35] and tip-enhanced Raman spectroscopy [36] show promise for measuring the strain in nanoscale regions. When the nanostructures being studied are embedded in a bulk, however, these techniques can have trouble separating the active region's signal from the bulk. I present here a new general spectroscopic technique for investigating strain and apply it to near-field imaging of nano-scale regions. This strain-mapping method compares theoretical modeling of electron-phonon interactions with phonon-replica intensities extracted from spectra to determine the strain. Our proposed technique is capable of measuring the strain of an active layer regardless of the material it is embedded within.

Elimination of growth defects in nanostructures requires techniques capable of effectively resolving strain variations and defects. Advances in techniques such as high-resolution X-ray diffraction (HR-XRD) and near-field Raman spectroscopy provide important tools for assessing the strain in a nanostructure. In light-emitting semiconductor quantum heterostructures it is common for doped binary semiconductors to provide the potential barrier for quantum confinement. In many cases the doping

required to produce a spectrally resolvable change in the bandgap can be small, and hence effective change in the lattice constant of the quantum structure compared to the surrounding material may be small. In these cases, techniques such as HR-XRD and Raman will measure both the strain of the embedding material (bulk) and the active region simultaneously. As the volume of the bulk tends to be significantly larger than the active region itself, the strain of the quantum structure can become lost in the signal of the bulk. In many cases, however, the quantum structure may be independently spectrally resolved from the bulk emission. This provides an opportunity for measuring the strain from spectral information retrieved directly from the active area.

One example of strain information in spectral data is the dependence of the energy of emission of excitons on strain in the sample. This energy shift may be measured and related directly the strain of the region of emission [37]. Generally, however, excitons can only be observed at low temperatures, increasing the complexity of such experiments for functional devices. Furthermore such measurements must take into account the change in the strain in the system at low temperatures [38].

#### 4.2 The Huang-Rhys Parameter ( $S$ )

In contrast to the exciton energy dependence, electron-phonon interactions become stronger at higher temperatures as the population of phonons increases [39]. In binary semiconductors with optical phonon modes, interaction between longitudinal optical (LO) phonons and electron-hole pairs can play a significant role in recombination. This results in "phonon-replicas" of the main emission, i.e. secondary peaks lowered in energy by an amount  $\Delta E = n \times \hbar\omega_{LO}$ , an integral multiple of the LO phonon energy. The intensities of subsequent replicas can be related directly to the

strength of electron-phonon interactions within the structure by the equation  $S = (n+1) I_{n+1}/I_n$  [31]. This parameter  $S$ , known as the Huang-Rhys parameter, is a measure of the energy of interaction between electrons and LO phonons [40] within the system and is dependent on the phonon frequencies of the materials used in the heterostructure [41]. Since it is well known that phonon-frequencies in materials experience strain related shifts [41-43], measured values of  $S$  contain information about the strain. To-date, both the empirical measurement of the Huang-Rhys parameter via photoluminescence measurements [44,45] and theoretical calculation [46-51] have been well established.

### 4.3 Calculating $S$

Before attempting to calculate the strain-dependent Huang-Rhys parameter  $S(\epsilon_{xx})$ , I will first demonstrate the calculation of  $S$  for our InGaN/GaN ELOG MQW structure. I have simplified the calculations by limiting the calculations to only include the interface LO (I-LO) phonon modes. This is possible in InGaN systems as it is known that the I-LO phonon modes account as much as 46% of the total electron-optical phonon interactions [51].

For the case of the I-LO phonon modes,  $S$  can be defined as [52]

$$S = (\hbar\omega_{LO}^3)^{-1} \sum_m \sum_{\mathbf{q}_\perp} |D_m(\mathbf{q}_\perp)|^2 \quad (4.3.1)$$

in which  $\omega_{LO}$  is the LO phonon frequency,  $D_m(\mathbf{q}_\perp)$  represents the difference between the strength of coupling of electrons and holes to the phonons and is given by [52]:

$$\mathcal{D}_m(\mathbf{q}_\perp) = \iiint d^2\mathbf{r} dz_e dz_h |\Psi(r, z_e, z_h)|^2 \left( \frac{2 \omega_m(\mathbf{q}_\perp)}{\hbar} \right)^{\frac{1}{2}} \times \left( e^{i\mathbf{q}_\perp \cdot \mathbf{r} (m_h/M)} \Gamma_m(\mathbf{q}_\perp, z_h) - e^{-i\mathbf{q}_\perp \cdot \mathbf{r} (m_e/M)} \Gamma_m(\mathbf{q}_\perp, z_e) \right) \quad (4.3.2)$$

There are three main components in Eq. 4.3.2 which need to be determined in order to calculate  $D_m(\mathbf{q}_\perp)$ , and hence  $S$ : The exciton wavefunction  $\Psi(r, z_e, z_h)$ , the phonon dispersion relation  $\omega_m(\mathbf{q}_\perp)$ , and the electron-phonon coupling strength  $\Gamma_m(\mathbf{q}_\perp, z_{e,h})$ .

#### 4.3.1 The Exciton Wavefunction

Let us begin by calculating the wavefunction of an e-h pair within an  $\text{In}_{0.20}\text{Ga}_{0.80}\text{N}/\text{GaN}$  QW. Solving for the wavefunction involves three steps, firstly calculating the electron and hole wavefunctions independently, then assuming a hydrogenic envelope wavefunction and minimizing the energy of the exciton to find the exciton Bohr radius.

As previously discussed in §2.4, wurtzite  $\text{InGaN}/\text{GaN}$  QWs exhibit an internal electric field which arises due to the piezoelectric nature of  $\text{InGaN}$ . This electric field is oriented along the  $c$ -axis of the structure which results in a non-square well potential. This “bending” of the potential in the QW due to the internal electric field is known as the quantum-confined Stark effect [22] and results in a spatial separation of the electron and hole wavefunctions as well as a decrease in the effective bandgap of the QW. In order to find the energies and wavefunctions of the electron and hole within the QW we must solve Schrodinger’s equation:



$$-\frac{\hbar}{2m}\nabla^2\psi(z) - \Phi(z)\psi(z) = \varepsilon \psi(z) \quad (4.3.3)$$

Due to the piezoelectric field within the QW, the value of  $\Phi$  changes with each region of the QW as follows:

$$\Phi_{e,h} = \begin{cases} \Delta E_{c,v} & z < -d_{qw} \\ -F_{pz}z & -d_{qw} \leq z \leq 0 \\ \Delta E_{c,v} - F_{pz}d_{qw} & z \geq 0 \end{cases} \quad (4.3.4)$$

Where  $\Delta E_{c,v} = \delta E_{c,v}$   $\Delta E_g = \delta E_{c,v}$  [ $E_g$  (GaN) –  $E_g$  (InGaN)] represents the division of the difference in bandgap energies between the conduction and valence bands. In our case I have used  $\delta E_c = 0.8$  and  $\delta E_v = 0.2$  [53]. Substituting Eq. 4.3.4 into 4.3.3 gives us the set of equations which we need to solve:

$$\begin{cases} -\frac{\hbar}{2m}\nabla^2\psi_I(z) + \Delta E_{c,v} \psi_I(z) = \varepsilon \psi_I(z) & z < -d_{qw} \\ -\frac{\hbar}{2m}\nabla^2\psi_{II}(z) + F_{pz}z \psi_{II}(z) = \varepsilon \psi_{II}(z) & -d_{qw} \leq z \leq 0 \\ -\frac{\hbar}{2m}\nabla^2\psi_{III}(z) - (\Delta E_{c,v} - F_{pz}d_{qw}) \psi_{III}(z) = \varepsilon \psi_{III}(z) & z \geq 0 \end{cases} \quad (4.3.5)$$

While Schrodinger's equation can be solved analytically for very few kinds of potential, the linear potential is one of those that can be. The solutions for a potential  $\Phi(z) = Fz + C$  take the form of a linear superposition of the Airy functions  $\text{Ai}(z)$  and  $\text{Bi}(z)$ :

$$\psi_{II}(z) = C \operatorname{Ai}\left(\frac{-\frac{2m(F_{pz}z + F_{pz}\varepsilon)}{\hbar^2}}{(-\frac{2mF_{pz}}{\hbar^2})^{2/3}}\right) + D \operatorname{Bi}\left(\frac{-\frac{2m(F_{pz}z + \varepsilon)}{\hbar^2}}{(-\frac{2mF_{pz}}{\hbar^2})^{2/3}}\right) \quad (4.3.6)$$

The solutions in the other two regions, as would be expected, take the form of exponential functions, such that the full wavefunction has the form

$$\psi(z) = \begin{cases} \mathcal{A} e^{\frac{z\sqrt{2m(\Delta E_{c,v}-\varepsilon)}}{\hbar}} + \mathcal{B} e^{-\frac{z\sqrt{2m(\Delta E_{c,v}-\varepsilon)}}{\hbar}} & z < -d_{qw} \\ C \operatorname{Ai}\left(\frac{-\frac{2m(F_{pz}z + F_{pz}\varepsilon)}{\hbar^2}}{(-\frac{2mF_{pz}}{\hbar^2})^{2/3}}\right) + D \operatorname{Bi}\left(\frac{-\frac{2m(F_{pz}z + \varepsilon)}{\hbar^2}}{(-\frac{2mF_{pz}}{\hbar^2})^{2/3}}\right) & -d_{qw} \leq z \leq 0 \\ \mathcal{E} e^{\frac{z\sqrt{2m(\Delta E_{c,v}-\varepsilon-F_{pz}d_{qw})}}{\hbar}} + \mathcal{F} e^{-\frac{z\sqrt{2m(\Delta E_{c,v}-\varepsilon-F_{pz}d_{qw})}}{\hbar}} & z \geq 0 \end{cases} \quad (4.3.7)$$

with the boundary conditions:

$$B.C.s = \begin{cases} \psi_I(-\infty) = 0; \psi_{III}(\infty) = 0 \\ \psi_I(-d_{qw}) = \psi_{II}(-d_{qw}); \psi_{II}(0) = \psi_{III}(0) \\ \frac{\partial}{\partial z} \psi_I(-d_{qw}) = \frac{\partial}{\partial z} \psi_{II}(-d_{qw}) \\ \frac{\partial}{\partial z} \psi_I(0) = \frac{\partial}{\partial z} \psi_{III}(0) \end{cases} \quad (4.3.8)$$

Fig. 4.1a depicts the band-structure of the QW we wish to find the solution of Schrodinger's equation for, while Table 4.1 presents the parameters used for calculating the band-structure and solving Eq. 4.3.4.

Table 4.1 Material parameters used for calculating the excitonic wavefunction.

	GaN	InN	In <sub>x</sub> Ga <sub>1-x</sub> N
$E_g$ (eV)	3.493 <sup>[54]</sup>	-	$(3.493 - 2.843x - 2.500x(1-x))^{[54]}$
$\xi$ (MV cm <sup>-1</sup> )	98 <sup>[14]</sup>	221 <sup>[14]</sup>	$(\xi_{GaN}(1-x) + \xi_{InN}x)^{[14]}$
$F_{pz}$ (MV cm <sup>-1</sup> )	-	-	$-\xi_{InGaN}\epsilon_{xx}(x)^{[14]}$

Here the Indium-fraction-dependent strain  $\epsilon_{xx}(x)$  is defined as  $(a_{GaN} - a_{InGaN})/a_{InGaN}$ ,

where  $a_{GaN}$  and  $a_{InGaN}$  are the unstrained lattice constants along the  $a$ -axis. This equation assumes that the InGaN has been grown pseudomorphic to the GaN, i.e. the thickness of the QW is small enough that the InGaN lattice has been uniformly compressed to match that of the GaN.

Solving Eq. 4.3.4 using the parameters in Table 4.1 and the boundary conditions

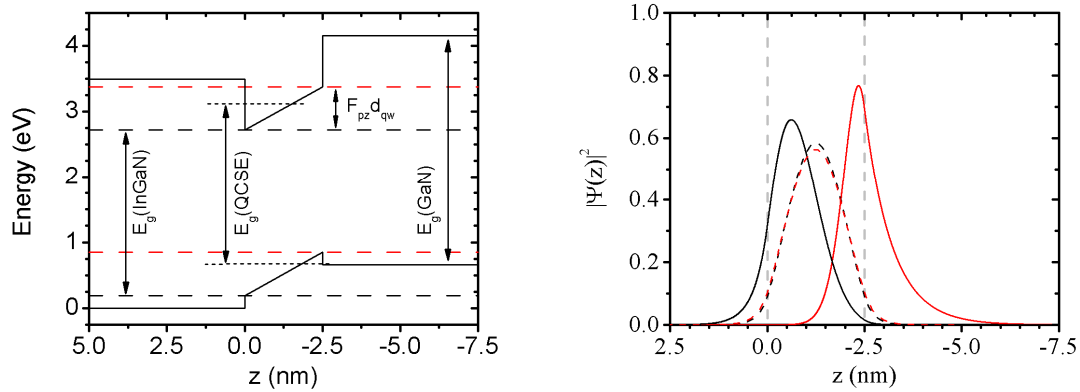


Figure 4.1 a, Band-structure diagram of a single 2.5 nm In<sub>0.20</sub>Ga<sub>0.80</sub>N/GaN QW. The black (red) dashed lines represent the InGaN bandgap before (after) the piezoelectric shift in energy  $F_{pz}d_{qw}$ . The dotted black lines represent the energy levels of the electron and hole, with the distance between them being the reduced bandgap due to the quantum-confined Stark effect. b, Wavefunctions of the electron (black) and hole (red) for the QW shown in in a. The dashed lines represent the solution for the same system with  $F_{pz} = 0$ .

presented in Eq. 4.3.5 gives a single energy level for the electron and hole at 402.5 and 176.3 meV above the InGaN bandgap respectively. By comparison, the first energy levels for a square well ( $F_{pz} = 0$ ) would be 141.6 and 30.1 meV respectively. While it would seem that the energies have in fact increased in the presence of the electric field, this is not the case. The bandgap before the application of the internal electric field is  $E_g + E_e + E_h = 2.524 \text{ eV} + 141.6 \text{ meV} + 30.1 \text{ meV} = 2.696 \text{ eV}$ . The bandgap in the presence of the piezoelectric field, however, is  $E_g + E_e + E_h - E_{pz} = 2.524 \text{ eV} + 402.5 \text{ meV} + 176.3 \text{ meV} - 656.9 \text{ meV} = 2.446 \text{ eV}$ . Therefore the presence of the internal piezoelectric field results in a red-shift in the emission energy of roughly 250 meV.

Using these calculated energies we can then calculate the various interface constants  $A$ - $F$ , and then normalize the wavefunctions such that  $\int \psi^*(z)\psi(z) dz = 1$ . Doing so yields the wavefunctions depicted in Figure 4.1b. I wish to point out here that the electron and hole wavefunctions have been separated to opposite sides of the QW by the internal electric field. This separation due to the QCSE is the origin of long decay lifetime found in InGaN/GaN QWs, as the recombination rate is proportional to the product of the electron and hole wavefunctions  $\psi_e(z_e) * \psi_h(z_h)$ , which is obviously significantly lower in the presence of the QCSE than for a square well.

Now that we have  $\psi_e(z_e)$  and  $\psi_h(z_h)$ , we may now calculate the full exciton wavefunction  $\Psi(r, z_e, z_h)$ . This is done using the method outlined in Ref [51]. We begin by assuming that the exciton wavefunction is separable into the electron and hole wavefunctions in the  $z$  direction, and a hydrogenic wavefunction in the plane perpendicular to  $z$ .

$$\Psi(r, z_e, z_h) = \mathcal{A} \psi_e(z_e) \psi_h(z_h) \varrho(r) \quad (4.3.9)$$

We choose  $\varrho(r) = \sqrt{2/a_0} e^{-r/a_0}$  as a trial wavefunction, and then minimize the energy of the exciton using the exciton Bohr radius  $a_0$  as the variational parameter:

$$\begin{aligned} E_{ex} &= \min_{a_0} \langle \Psi | H | \Psi \rangle \\ &= \min_{a_0} \left[ \iiint \Psi^* \left( H_e + H_h - \frac{e^2}{\epsilon \sqrt{r^2 + (z_e - z_h)^2}} \right) \Psi \, dr \, dz_e \, dz_h \right] \end{aligned} \quad (4.3.10)$$

While this minimization problem seems quite complex, it turns out that the only portion of the integral which varies with  $a_0$  is the excitonic portion of the Hamiltonian,  $-e^2/\epsilon|r|^2$ . The other parts of the Hamiltonian depend only upon the  $z$  components of the

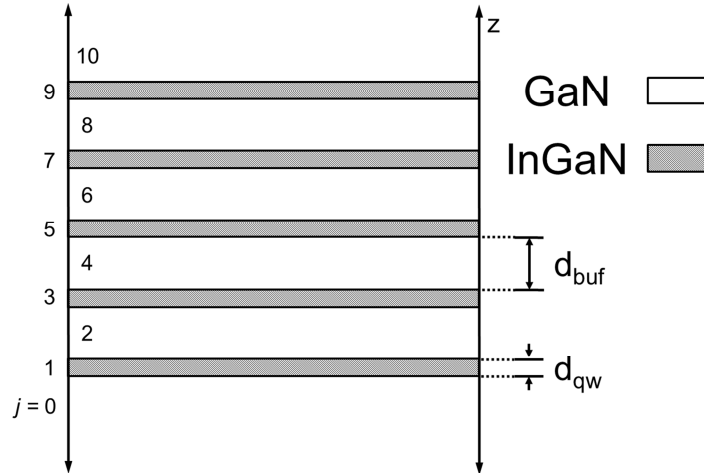


Figure 4.2 Schematic diagram of the structure used for the dispersion calculations. The numbers on the left represent the indices used for the matrix of each region of the heterostructure.

exciton wavefunction, and hence the  $r$  component of the wavefunction may be separated out resulting in the integral  $\int \psi^* \psi \, dr = 1$ .

#### 4.3.2 The Phonon Dispersion Relation

Next we need to calculate the phonon dispersion relation  $\omega_m(\mathbf{q}_\perp)$  for the I-LO phonon modes within our heterostructure. Our InGaN/GaN ELOG samples consist of 5 x 2.5 nm QWs separated by 7.5 nm buffers. The multi-QW is capped on the top by a 20 nm cap layer, and sits atop a 500  $\mu\text{m}$  GaN buffer layer. In order to simplify the equations, I have assumed that both the top and bottom layers are semi-infinite. The diagram in Figure 4.2 represents the heterostructure used for the phonon dispersion calculations.

The problem of solving for the dispersion of I-LO phonons in a heterostructure super-lattice such as the QW has previously been solved for a generic III-V heterostructure super-lattice [40]. I present, in the next few sections, a summary of the method presented in that work.

The polarization  $P_{\text{perp}}(z)$  induced by a phonon with wavevector  $q_{z,j}$  in layer  $j$  of the heterostructure obeys the following second-order ODE:

$$\frac{d^2}{dz^2} P_\perp^{(j)}(z) + q_{z,j}^2 P_\perp^{(j)}(z) = 0 \quad (4.3.11)$$

with solutions of the form:

$$P_{\perp}^{(j)}(z) = i(\mathcal{A}_j e^{i q_{z,j}(z-z_j)} + \mathcal{B}_j e^{-i q_{z,j}(z-z_j)}) \quad (4.3.12)$$

For I-OP modes, the  $z$ -component of the wavevector is imaginary, meaning that the solutions for the polarization take the form of a linear superposition of an exponential growth and decay term. If we substitute  $i q_{z,j}$  for  $q_{z,j}$  in Eq. 4.3.12 we can see that for the region  $j=0$  which runs from  $-\infty$  to 0,  $\mathcal{A}_0$  must be zero such that  $P_{\perp}(-\infty) = 0$ . Similarly,  $\mathcal{B}_{10} = 0$  so that  $P_{\perp}(\infty) = 0$ .

For the remaining coefficients, we can relate the coefficients  $\mathcal{A}$  and  $\mathcal{B}$  of layer  $j$  to those of layer  $j+1$  by using the electrostatic boundary conditions for the polarization at the  $z_j$  interface:

$$\begin{aligned} \chi_{\perp,j}^{-1}(\omega) P_{\perp}^{(j)}(z) \Big|_{z=z_j} &= \chi_{\perp,j+1}^{-1}(\omega) P_{\perp}^{(j+1)}(z) \Big|_{z=z_j} \\ \frac{\epsilon_{z,j}(\omega)}{\chi_{z,j}(\omega)} P_z^{(j)}(z) \Big|_{z=z_j} &= \frac{\epsilon_{z,j+1}(\omega)}{\chi_{z,j+1}(\omega)} P_z^{(j+1)}(z) \Big|_{z=z_j} \end{aligned} \quad (4.3.13)$$

The application of the BCs results in the following set of matrix relations for the coefficients:

$$\begin{aligned}
\begin{pmatrix} \mathcal{A}_{j+1} \\ \mathcal{B}_{j+1} \end{pmatrix} &= M_j \begin{pmatrix} \mathcal{A}_j \\ \mathcal{B}_j \end{pmatrix}, \quad j = 0..9 \\
M_j &= \frac{1}{2} \begin{pmatrix} (1 + \alpha_{j,j+1})\beta_{j,j+1}e^{-q_{z,j+1}d_{j+1}} & (1 - \alpha_{j,j+1})\beta_{j,j+1}e^{-q_{z,j+1}d_{j+1}} \\ (1 - \alpha_{j,j+1})\beta_{j,j+1}e^{q_{z,j+1}d_{j+1}} & (1 + \alpha_{j,j+1})\beta_{j,j+1}e^{q_{z,j+1}d_{j+1}} \end{pmatrix} \\
M_9 &= \frac{1}{2} \begin{pmatrix} (1 + \alpha_{j,j+1})\beta_{j,j+1} & (1 - \alpha_{j,j+1})\beta_{j,j+1} \\ (1 - \alpha_{j,j+1})\beta_{j,j+1} & (1 + \alpha_{j,j+1})\beta_{j,j+1} \end{pmatrix} \\
\alpha_{j,j+1} &\equiv \frac{q_{z,j}\epsilon_{z,j}(\omega)}{q_{z,j+1}\epsilon_{z,j+1}(\omega)}; \quad \beta_{j,j+1} \equiv \frac{\chi_{\perp,j+1}(\omega)}{\chi_{\perp,j}(\omega)}
\end{aligned} \tag{4.3.14}$$

The dispersion relation can then be found by relating the  $j=0$  coefficients to the  $j=10$  coefficients. Doing so yields:

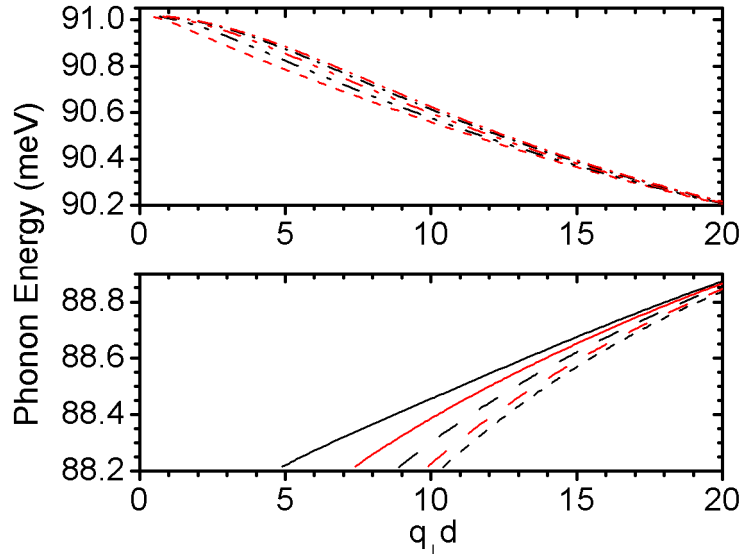


Figure 4.3 Plots of the dispersion relations for the upper and lower branches of the I-LO phonon modes for the heterostructure pictured in Fig 4.2. The 10 modes arise from zone-folding of the phonons at the super-lattice interfaces. Black (red) lines represent the (anti-)symmetric phonon modes.



$$\begin{pmatrix} \mathcal{A}_{10} \\ 0 \end{pmatrix} = M_9 M_8 \dots M_0 \begin{pmatrix} 0 \\ \mathcal{B}_0 \end{pmatrix} = \mathcal{M} \begin{pmatrix} 0 \\ \mathcal{B}_0 \end{pmatrix} \quad (4.3.15)$$

Of which the component  $\mathcal{M}_{2,2} \mathcal{B}_0 = 0$  provides us with the dispersion relation. Since  $\mathcal{B}_0 = 0$  would result in a trivial solution the modes must be described by  $\mathcal{M}_{2,2} \neq 0$ . As this equation for the dispersion relation has no analytical solutions, so the solutions were found using numerical methods. Figure 4.3 shows the calculated solutions using the parameters presented in Table 4.2.

Table 4.2 Material parameters used to calculate the phonon dispersion relation. InN and GaN values from Ref. [52], InGaN values calculated using Vegard's Law.

	GaN	InN	In <sub>0.2</sub> Ga <sub>0.8</sub> N
A <sub>1</sub> [LO] (meV)	91.02	72.65	87.33
E <sub>1</sub> [LO] (meV)	91.88	73.52	88.20
A <sub>1</sub> [TO] (meV)	65.94	55.42	63.83
E <sub>1</sub> [TO] (meV)	69.29	59.02	67.23
$\epsilon_z^{(0)}$	9.2	15.3	10.42
$\epsilon_z^{(\infty)}$	5.32	8.4	5.96

#### 4.3.3 $\mathcal{A}_j, \mathcal{B}_j$ – The Interface Constants

The step in calculating S is obtaining the interface constants used in the transfer matrices in Eqs. 4.3.14 and 4.3.15. Per Ref. [40], the constants in Eq. 4.3.14 may all be rewritten in terms of one constant,  $\mathcal{B}_0$  as such:

$$\begin{aligned}\mathcal{A}_j &= \mathcal{A}'_j \mathcal{B}_0 \\ \mathcal{B}_j &= \mathcal{B}'_j \mathcal{B}_0\end{aligned}\tag{4.3.16}$$

This allows us to solve for the primed constants using Eq. 4.3.14.  $\mathcal{B}_0$  in turn, is given by

$$\begin{aligned}\mathcal{B}_0 &= \sqrt{\frac{2}{\Lambda}} \\ \Lambda &\equiv \frac{1}{q_{z,0}} \mathcal{Q}_{0,+}(\omega) + \frac{\mathcal{A}'_{N+1}{}^2}{q_{z,N+1}} \mathcal{Q}_{N+1,+}(\omega) \\ &\quad + \sum_{j=1}^N \frac{1}{q_{z,j}} \{ 4 \mathcal{A}'_j \mathcal{B}'_j q_{z,j} d_j \mathcal{Q}_{j,-}(\omega) \\ &\quad - [\mathcal{A}'_j{}^2 (1 - e^{2q_{z,j}d_j}) - \mathcal{B}'_j{}^2 (1 - e^{2q_{z,j}d_j})] \mathcal{Q}_{j,+}(\omega) \}\end{aligned}\tag{4.3.17}$$

$$\begin{aligned}\mathcal{Q}_{j,\pm}(\omega) &\equiv \frac{\eta_{\perp,j}(\omega)}{\omega_{\perp,pj}^2} \pm \gamma_j^2 \frac{\eta_{z,j}(\omega)}{\omega_{z,pj}^2} \\ \frac{\eta_{\chi,j}(\omega)}{\omega_{\chi,pj}^2} &= \frac{(\epsilon_{\chi,j}(\omega) - \epsilon_{\chi,j}^{(\infty)})^2}{\omega_{\chi,Tj}^2 (\epsilon_{\chi,j}(\omega) - 1) [\epsilon_{\chi,j}^{(0)} - \epsilon_{\chi,j}^{(\infty)}]^2}\end{aligned}$$

where  $\epsilon_{\chi,j}^{(\infty)}$  and  $\epsilon_{\chi,j}^{(0)}$  are the optical and static dielectric constant in layer  $j$  in the direction of  $\chi$  respectively.

#### 4.3.4 $\Gamma$ – The Electron-Phonon Coupling Strength

The final thing that needs to be computed in order to obtain a value for  $S$  is the electron-phonon coupling function  $\Gamma$ . For this calculation we have used the equation for  $\Gamma$  for the I-LO modes presented in Ref. [40]. In this case  $\Gamma_m(\mathbf{q}_{\perp}, \mathbf{z}_{e,h})$  is given as:

$$\Gamma_m(\mathbf{q}_\perp, z_{e,h}) = \mathcal{B}_0 \left( \frac{\hbar e^2}{8 A \epsilon_0 \omega_m(\mathbf{q}_\perp)} \right)^{1/2} \begin{cases} f_1(\mathbf{q}_\perp, z) & z < z_0 \\ f_2(\mathbf{q}_\perp, z) & z_{j-1} \leq z \leq z_j, \\ f_3(\mathbf{q}_\perp, z) & z > z_9 \end{cases} \quad j = 1..9 \quad (4.3.16)$$

where  $e$  is the fundamental charge,  $\hbar$  the reduced Planck's constant,  $\epsilon_0$  the permittivity of free space, and  $A$  the cross-sectional area of the heterostructure. I point out that the phonon dispersion relation  $\omega_m(\mathbf{q}_\perp)$  enters here as well as directly in the calculation for  $S$ .

The functions  $f_i$  are given as:

$$\begin{aligned} f_1(q_\perp, z) &\equiv \xi_{-,0} e^{q_\perp(z-z_0)} + (\xi_{+,0} - \xi_{-,0}) e^{q_{z,0}(z-z_0)} \\ &+ \sum_{\ell=1}^N [(\mathcal{A}_\ell \xi_{+,\ell} e^{q_{z,\ell} d_\ell} - \mathcal{B}_\ell \xi_{-,\ell} e^{-q_{z,\ell} d_\ell}) e^{q_\perp(z-z_{\ell-1})} \\ &+ (\mathcal{B}_\ell \xi_{-,\ell} - \mathcal{A}_\ell \xi_{+,\ell}) e^{q_\perp(z-z_\ell)}] + \mathcal{A}_{N+1} \xi_{+,N+1} e^{q_\perp(z-z_N)} \\ f_{2,j}(q_\perp, z) &\equiv \xi_{-,0} e^{q_\perp(z-z_0)} \\ &+ \sum_{\ell=1}^{j-1} [\mathcal{A}_\ell \xi_{-,\ell} e^{q_{z,\ell} d_\ell} - \mathcal{B}_\ell \xi_{+,\ell} e^{-q_{z,\ell} d_\ell} \\ &+ (\mathcal{B}_\ell \xi_{+,\ell} - \mathcal{A}_\ell \xi_{-,\ell}) e^{q_\perp d_\ell}] e^{q_\perp(z_{\ell-1}-z)} \\ &+ (\mathcal{A}_j \xi_{-,j} e^{q_{z,j} d_j} - \mathcal{B}_j \xi_{+,j} e^{-q_{z,j} d_j}) e^{q_\perp(z_{j-1}-z)} \\ &+ (\xi_{+,j} - \xi_{-,j}) (\mathcal{A}_j e^{q_{z,j}(z_j-z)} + \mathcal{B}_j e^{q_{z,j}(z-z_j)}) \\ &+ (\mathcal{B}_j \xi_{-,j} - \mathcal{A}_j \xi_{+,j}) e^{q_\perp(z-z_j)} \\ &+ \sum_{\ell=j+1}^N [\mathcal{A}_\ell \xi_{+,\ell} e^{q_{z,\ell} d_\ell} - \mathcal{B}_\ell \xi_{-,\ell} e^{-q_{z,\ell} d_\ell} \\ &+ (\mathcal{B}_\ell \xi_{-,\ell} - \mathcal{A}_\ell \xi_{+,\ell}) e^{q_\perp d_\ell}] e^{q_\perp(z-z_{\ell-1})} + \mathcal{A}_{N+1} \xi_{+,N+1} e^{q_\perp(z-z_N)} \end{aligned} \quad (4.3.17)$$

$$\begin{aligned}
\mathcal{F}_3(q_\perp, z) &\equiv \xi_{-,0} e^{q_\perp(z_0-z)} \\
&+ \sum_{\ell=1}^N [\mathcal{A}_\ell \xi_{-, \ell} e^{q_{z,\ell} d_\ell} - \mathcal{B}_\ell \xi_{+, \ell} e^{-q_{z,\ell} d_\ell} + (\mathcal{B}_\ell \xi_{+, j} \\
&- \mathcal{A}_\ell \xi_{-, \ell}) e^{q_\perp d_\ell}] e^{q_\perp(z_{\ell-1}-z)} + \mathcal{A}_{N+1} [\xi_{+, N+1} e^{q_{z, N+1}(z_N-z)} \\
&+ \xi_{-, N+1} (e^{q_\perp(z_N-z)} - e^{q_{z, N+1}(z_N-z)})]
\end{aligned} \tag{4.3.17}$$

(cont'd)

where  $\xi_{\pm, j}$  is defined to be:

$$\begin{aligned}
\xi_{\pm, j} &\equiv \frac{1 \pm \gamma_j}{q_{z, j} \pm q_\perp} \\
\gamma_j &\equiv \frac{q_{z, j} \chi_{z, j}(\omega)}{q_\perp \chi_{\perp, j}(\omega)}
\end{aligned} \tag{4.3.18}$$

Eqs. 4.3.16-18 along with the dispersion relation then allow us to compute the value of  $\Gamma$  for our heterostructure. Figure 4.4 shows the upper and lower branches of  $\Gamma$

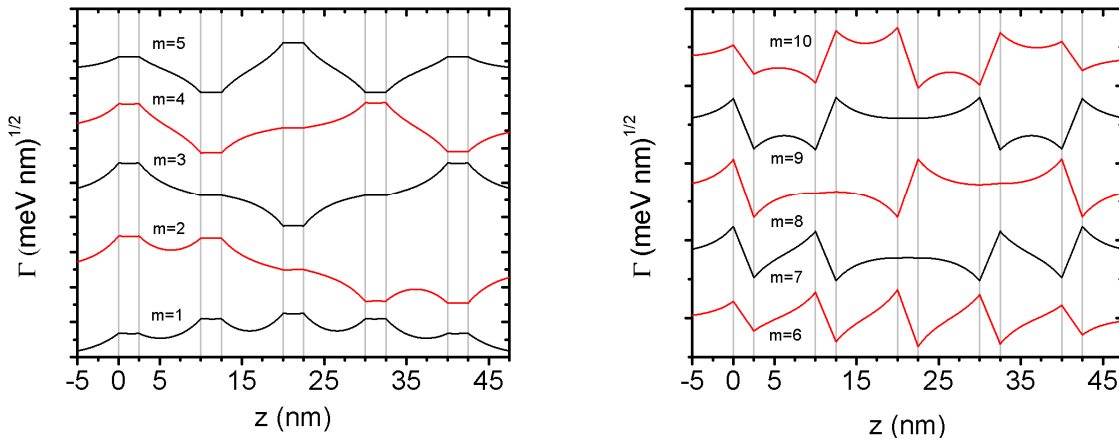


Figure 4.4 a, Lower branches of  $\Gamma_m(q_\perp, z_{e,h})$  with the symmetric solutions in black and anti-symmetric in red with the associated mode number. b, Upper branches of the same.

as a function of position within the heterostructure.

#### 4.4 S and Strain

The Huang-Rhys parameter  $S$  then can be calculated by substituting the results of the calculations of  $\omega_m(\mathbf{q}_\perp)$  and  $\Gamma_m(\mathbf{q}_\perp, z_{e,h})$  along with the exciton wavefunction  $\Psi$  into Eq. 4.3.2 and then into Eq. 4.3.1. While this gives us a value of  $S$  for the system, I have not explained yet how to derive  $S$  as a function of the biaxial strain  $\epsilon_{xx}$  for the system. In these equations the phonon frequency enters via the phonon dispersion relation  $\omega_m(\mathbf{q}_\perp)$  in both  $\Gamma_m(\mathbf{q}_\perp, z_{e,h})$  and  $S$  itself. The phonon frequencies in the system are a function of the strain and change at a rate proportional to the phonon deformation potentials (PDPs)  $a_\lambda$ ,  $b_\lambda$  for a given phonon mode. The change in the phonon frequency of mode  $\lambda$  is given as  $\Delta\omega_\lambda = 2 a_\lambda \epsilon_{xx} + b_\lambda \epsilon_{zz}$ , assuming that  $\epsilon_{yy} = \epsilon_{xx}$  [41]. If the QW has been grown pseudomorphic to the GaN then we can assume biaxial strain and can thereby relate the two remaining strain components in the active region as such  $\epsilon_{zz} = 2 \epsilon_{xx} C_{31}/C_{33}$  [27]. Together these allow us to define  $\Delta\omega_\lambda(\epsilon_{xx}) = 2(a_\lambda + b_\lambda C_{31}/C_{33}) \epsilon_{xx}$ , i.e. the change in phonon frequency as a function of the biaxial strain in the system. In our system, the relevant phonon modes for the I-LO phonon interactions are the  $A_1[\text{LO}]$  and  $E_1[\text{LO}]$  modes. For our calculations I have derived the  $A_1[\text{LO}]$  and  $E_1[\text{LO}]$  PDPs using a "Vegard's Law"-like formula from published values of the PDPs for GaN and InN. Since the  $E_1[\text{LO}]$  and  $A_1[\text{LO}]$  mode PDPs for InN are poorly covered in the literature, I have instead used the PDPs for the  $E_2^H$  mode and the method described by Briot, et al. [27] for relating  $\Delta\omega_{E_1[\text{LO}]}$  to  $\Delta\omega_{E_2^H}$ . Table 4.3 lists the values of the PDPs for the modes used in our calculations of  $S(\epsilon_{xx})$ .

It is important to point out that the strain also affects  $S$  through the wavefunction calculations as well. Specifically, the piezoelectric constant  $F_{pz} = -\xi_{InGaN} \epsilon_{xx}$  is a function of the strain in the system. Increasing or decreasing the strain will serve to increase the separation of the electron and hole portions of the exciton wavefunction within the QW.

Table 4.3 The PDPs and other parameters necessary to derive the strain-dependent phonon dispersion relations. Asterisks represent those parameters instead derived using Ref. [27].

	GaN	InN	In <sub>x</sub> Ga <sub>1-x</sub> N
$a_0$ (Å)	3.189 <sup>[48]</sup>	3.548 <sup>[48]</sup>	
$a_{A_1[LO]}, b_{A_1[LO]}$ (cm <sup>-1</sup> )	-847, -903 <sup>[49]</sup>	-944, -750 <sup>[42]</sup>	
$a_{E_1[LO]}, b_{E_1[LO]}$ (cm <sup>-1</sup> )	-775, -703 <sup>[43]</sup>	*	
$a_{A_1[TO]}, b_{A_1[TO]}$ (cm <sup>-1</sup> )	-664, -1182 <sup>[43]</sup>	*	
$a_{E_1[TO]}, b_{E_1[TO]}$ (cm <sup>-1</sup> )	-820, -680 <sup>[41]</sup>	-735, -644 <sup>[41]</sup>	
$a_{E_2^H}, b_{E_2^H}$ (cm <sup>-1</sup> )	-	-998, -635 <sup>[42]</sup>	
$C_{13} / C_{33}$	0.229 <sup>[42]</sup>	0.470 <sup>[42]</sup>	$0.229 (1 - x) + 0.470 x$

Since it is impossible to derive an analytical function for  $S(\epsilon_{xx})$ , I have produced

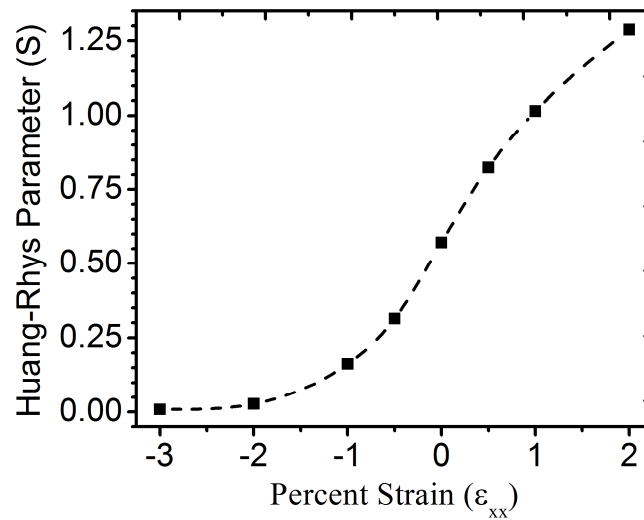


Figure 4.5 The Huang-Rhys parameter  $S$  as a function of the biaxial strain  $\epsilon_{xx}$  in the system.

an approximation of the function by computing  $S$  for varying values of the biaxial strain  $\epsilon_{xx}$ , and then interpolating the missing values using a cubic spline. For simplicity I have assumed that the wavefunction is a weak function of the strain and hence neglected the change in  $\Psi$  as a function of  $\epsilon_{xx}$ . Figure 4.5 shows the results of these calculations, which can now be used to convert experimentally measured values of  $S$  into the biaxial strain  $\epsilon_{xx}$ .

#### 4.5 Application: Near-field Strain Mapping

To test the efficacy of this technique, we used an InGaN/GaN multi-quantum well (MQW) structure grown via epitaxial layer overgrowth (ELOG). The ELOG technique uses apertures in an  $\text{SiO}_2$  mask to restrict the growth of GaN to "seed" regions [55]. Growth is continued through these openings and once above the mask growth continues normal to the substrate in the seed regions and parallel to it in the masked

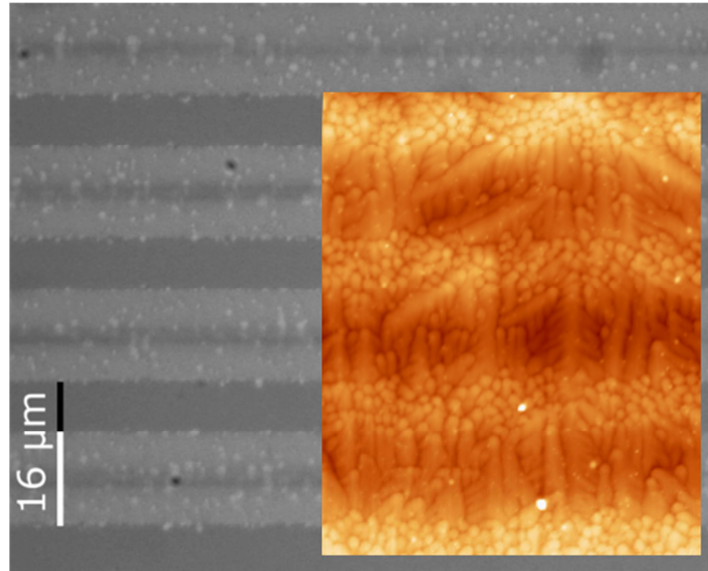


Figure 4.6 Top-down images of the ELOG sample showing the 'wing' and 'seed' regions of the sample. Imaging was done with an optical microscope using a 100x objective, and via AFM for the inset.

"wing" regions. These wing regions experience strain relaxation during growth and so have a lower overall strain than the GaN in the seed areas. The growth process is further detailed in §2.3.1. Figure 4.6 depicts the seed and wing regions as imaged using an optical microscope as well as AFM. Having been studied before [56], this controlled wide-area strain variation provides an excellent baseline for testing our strain mapping method. In order to extract  $S$  empirically, near-field photoluminescence (PL) measurements were conducted using a near-field scanning optical microspectrometer (NSOM) over a  $45 \times 45 \mu\text{m}$  region of the sample. At each measurement point, the spectrum was fitted using the method described in §3.7.

This fitting allows for the extraction of various parameters at each measurement point including the phonon replica intensities, which are then used to calculate  $S$  empirically according to the previously given equation  $S = (n+1) I_{n+1}/I_n$ . Furthermore, I was able to simultaneously map the topology of the system to allow me to associate the emission with the seed and wing regions. Figure 4.7 depicts the extracted parameters, including the max intensity and  $S$ , along with the near-field topology. As can be seen in panel d of Figure 4.7, there are regions near the center of each wing region which are relaxed compared to the seed regions. It is interesting to note that the majority of relaxation appears to occur at the boundary where the two halves of the wing region meet. It is unclear as to whether this is a result of the way growth proceeds when the two facets meet, or whether it is a direct result of the gradual relaxation that should occur as they grow away from the seed regions.

While the strain map in Figure 4.7d agrees well qualitatively with the expected variations, the values for strain produced from the theoretical model are around -0.2%



while one would expect a strain of around -2% in the studied system. This discrepancy arises primarily from our neglect of the other optical phonon modes which contribute to the electron-phonon coupling in the InGaN/GaN system. Specifically, the modes I have considered, the quasi-confined LO phonon modes, are only one of 5 different mode-types expected in the system. Additionally, uncertainty in the PDPs is likely to further contribute to the observed discrepancy.

The solution to these discrepancies is to first expand the calculations to include all the relevant modes. Secondly it would be ideal to use a secondary technique to measure the strain in the system, allowing us to compare and correct the model as necessary. A technique such as near-field raman spectroscopy would complement this strain-mapping technique well, as it can produce a direct measurement of the strain more directly by measuring the phonon frequencies, but is incapable of separating out the strain within the active layer from the strain of the cap and buffer layers. By using both techniques within the same region it would be possible to compare the strain of the active layer directly to the strain of the surrounding buffer materials, allowing for the discovery of defects within the active layer which do not extend into the surrounding buffer layers.

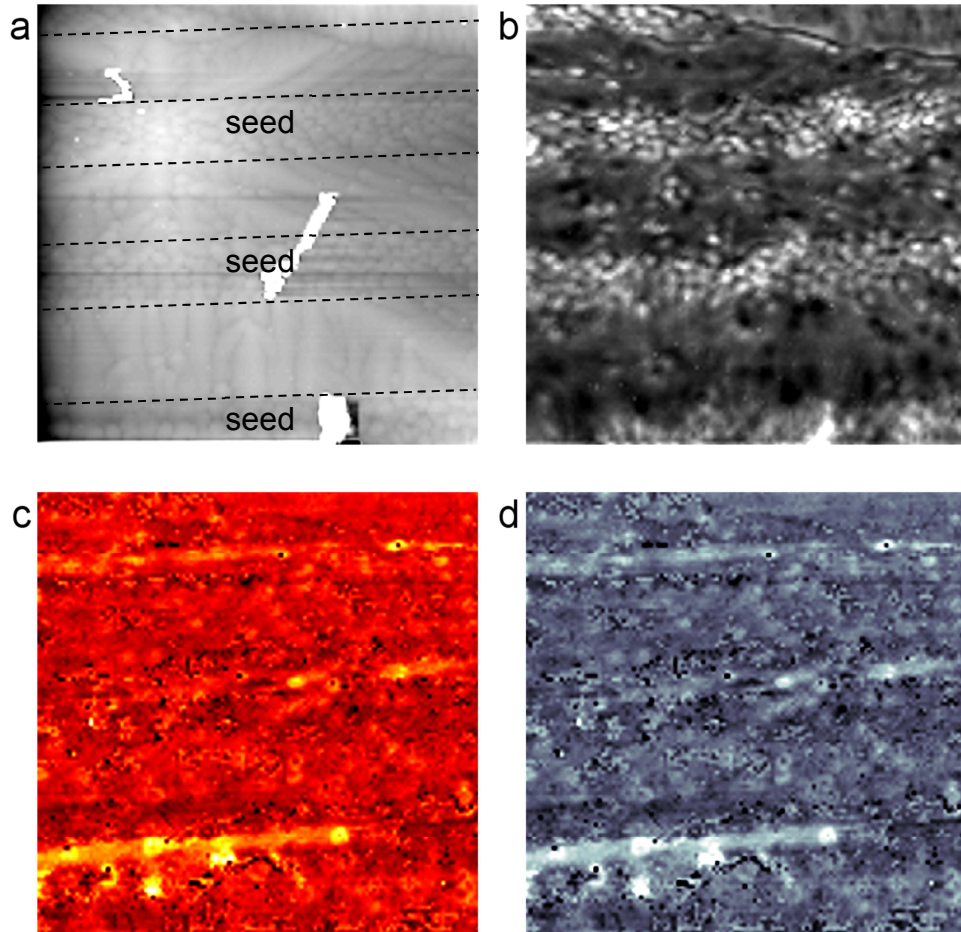


Figure 4.7 a, Near-field topology of the sample showing the ‘wing’ and ‘seed’ regions. Dashed lines have been placed to highlight the region boundaries. b, Near-field integrated photoluminescence intensity. Note that in this sample the emission intensity is highest in the seed regions. c, The empirically derived Huang-Rhys parameter. d, The strain as derived using the inverse of the function  $S(\epsilon_{xx})$  presented in Fig. 4.5. Brighter regions represent areas with lower strain values.

#### 4.6 Summary and Future Work

In conclusion I have presented here a new technique for extracting strain information from the spectra of optically active regions of a sample. Combining experimental data with theoretical modeling, this general spectroscopic technique can be coupled with near-field microscopy in order to image the strain in light-emitting nanostructures. The simultaneous measurement of strain and optical emission characteristics provided by our strain mapping technique allows for an in-depth analysis of the system being studied.

Further work on this topic is needed to improve the calculations. Firstly, it is important to go back and include all the optical phonon modes in the calculation, instead of only considering the I-LO phonon modes. Secondly, it is imperative to include in the exciton calculations the effects of the strain-dependent piezoelectric constant. Finally, this technique needs to be expanded to include other geometries, including quantum

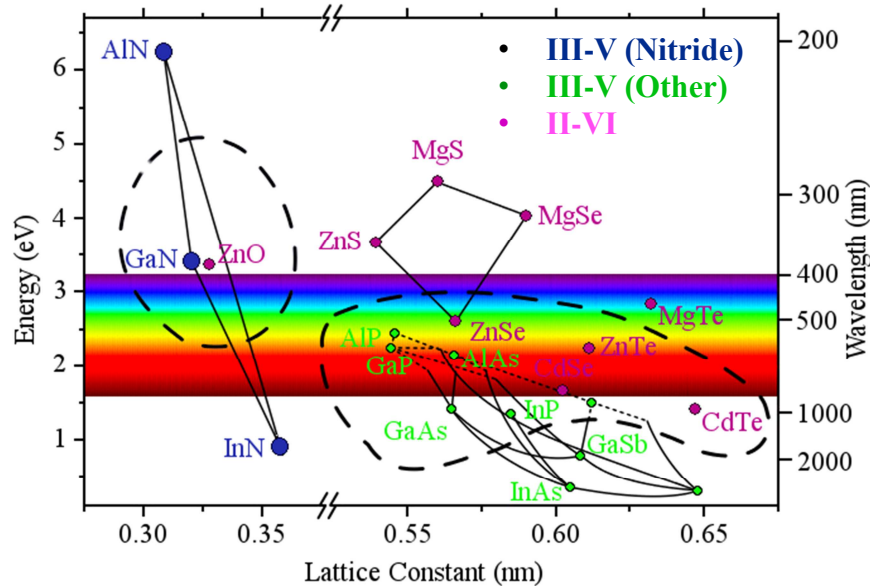


Figure 4.8 Emission energy of common semiconductors versus their lattice constants. The regions circled by the black dashed lines represent semiconductors known to exhibit phonon replicas.

wires and quantum dots, as well as more complex heterostructures such as those used in commercial LEDs. If this is done, this strain mapping technique should be applicable to all semiconductor light-emitters which exhibit phonon replicas in their PL spectra. This includes a wide range of common light-emitters, and many of those that are currently under investigation for future applications. Figure 4.8 shows a map of those semiconductors which are currently known to exhibit phonon replicas.

## CHAPTER 5

### THE IMAGE CHARGE EFFECT

#### 5.1 Emission Enhancement and Applied Plasmonics

The current understanding of semiconductor carrier dynamics in the vicinity of metals operates on the assumption that the interactions present are primarily electrodynamic in nature. This interaction is described by the coupling of carriers to the evanescent field of surface plasmon polaritons (SPPs) or localized surface plasmons (LSPs). For an InGaN/GaN multi-QW system, Aluminum (Al) and Silver (Ag) are typically used to produce a plasmonic interaction, since their plasmon resonances line up well with the typical energies of emission of InGaN heterostructures. In these cases Gold (Au) is generally used as a foil, to demonstrate through lack of enhancement that the enhancement is dependent on plasmon resonance and not simply due to the presence of a metal [6, 57].

One of the common issues with producing plasmonic enhancement in functional light-emitting devices (LEDs) is the need to grow a p-type layer for electrical contact above the multi-QW which acts as the source of light. Because of limitations in growth technology, the p-type layer generally needs to be thick enough (>200nm) that it becomes difficult to couple the SPPs in a metal thin-film to the carriers in the multi-QW. Various approaches have been tried to-date to bypass this problem [58-60]. One of these approaches, the experimental results of which I discuss here, involves the implantation of metallic nanoparticles (NPs) into the inverted hexagonal pits (IHPs) that occur naturally within InGaN/GaN multi-QW systems [61]. By making use of the IHPs it

should be possible to grow a p-type layer of the appropriate thickness without increasing the distance between the carriers and the NPs.

## 5.2 Anomalous Photoluminescence Results

When attempting to demonstrate plasmonic interaction in a metal/semiconductor structure, it is common to first search for enhancement in the CW photoluminescence (PL). I have investigated the CW PL emission in these nanoparticle samples using a reference (NP-less) sample as well as samples with Au and Ag nanoparticles. The results of these PL measurements are presented in Figure 5.1a. By way of comparison, I provide the results of a CW PL measurement of a similar InGaN/GaN multi-QW system with a metal thin-film (Au and Ag) along with a reference in Figure 5.1b. It is immediately obvious that while the intensity of the thin-film samples behaves as would be expected for plasmonic interaction, the NP samples exhibit anomalous behavior. Specifically, enhancement is produced in the presence of Au NPs, which cannot be

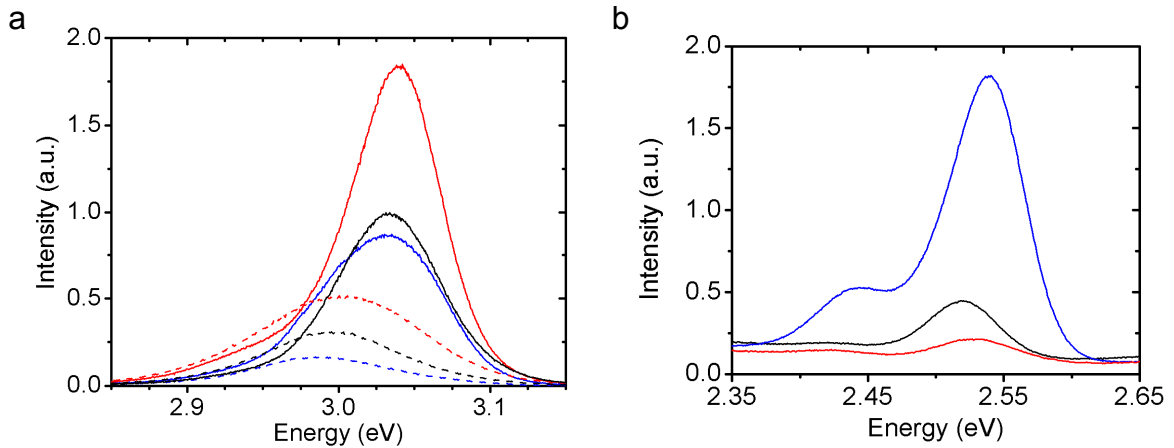


Figure 5.1 a, CW PL measurement of InGaN/GaN multi-QW system with embedded Au NPs (Red), Ag NPs (blue) and without NPs (black) at 77K (solid) and 300K (dashed). Note the anomalous increase in emission intensity due to the Au NPs. b, CW PL measurement for a similar structure with metal thin-films. Line colors are the same as those in a.

accounted for by plasmonic interaction due to the plasmon energy of the Au NPs being lower than the energy of the QW (2.3 eV vs 3 eV [57]).

Further evidence that plasmonics do not play a role in the measured PL enhancement is provided by time-resolved PL measurements of the samples. The results of these measurements, taken at 11K with an excitation power of 10 mW, can be found in Figure 5.2. In InGaN, it has been observed that plasmonic enhancement is accompanied by a decrease in the radiative recombination lifetime of up to two orders of magnitude [57]. This decrease is the result of rapid recycling of carriers due to resonant SP-carrier coupling. This reduction is a signature of plasmonic interaction and is the cause of the strong enhancement observed in the PL. Contrary to the case of plasmonics, the radiative recombination lifetime of the system appears to increase in the presence of both the Au and Ag NPs.

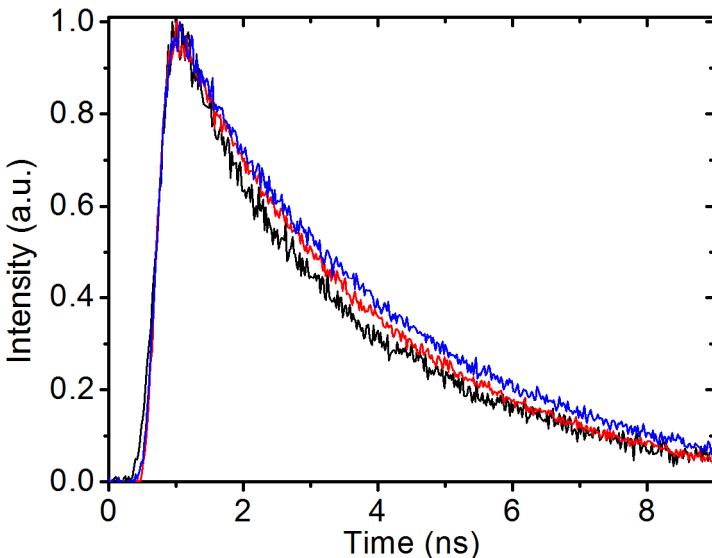


Figure 5.2 Time-resolved PL measurement showing the decay lifetime of the reference (black), Au NP (red) and Ag NP (blue) samples.

### 5.3 The Image Charge Effect

It is clear from the anomalous PL enhancement and the increase in the radiative decay lifetime of the system that SPs cannot be interaction mechanism present in the Au NP sample. There must instead be a mechanism of interaction between carriers and a metal

NP which is non-resonant and yet still produces enhancement. A possible candidate for this interaction is the electrostatic attraction between the carriers and the image charges they induce within the metal NPs. I hypothesize that this effect, hereafter referred to as the “Image Charge Effect”, is responsible not only for the enhanced PL and increased decay lifetime, but also for several other interesting features that I have demonstrated via experiments to be present in the non-resonant Au NP system.

For emission enhancement to occur one of two things must happen: Either there is some process which increases light extraction from the semiconductor, i.e. allows modes that would be trapped within the semiconductor due to total internal reflection to escape, or there must be some process that increases the internal quantum efficiency (IQE) of the system. In the Au NP system, the primary mechanism that could be responsible for increased light extraction from the semiconductor would be the scattering of light by the Au NPs. Similar to the plasmonic interaction, scattering effects may be ruled out in the case of Au NPs because the scattering cross-section of the Au NPs is negligible at the emission wavelength of the QW.

The IQE of semiconductor light emitters depends primarily on the radiative electron-hole recombination rate,  $\Gamma_{\text{radiative}}$ . The IQE can be defined as the ratio of radiative recombination events to total recombination events:

$$\eta = \frac{\Gamma_{\text{radiative}}}{\Gamma_{\text{non-radiative}} + \Gamma_{\text{radiative}}} \quad (5.3.1)$$

It is also known that, for semiconductors, both  $\Gamma_{\text{radiative}}$  and  $\Gamma_{\text{non-radiative}}$  depend upon the concentration  $n$  of excited carriers within the QW [62]. In terms of the carrier concentration Eq. 5.3.1 can be rewritten as [63]:



$$\eta = \frac{B n^2}{A n + B n^2 + C n^3} \quad (5.3.2)$$

Here  $B$  is proportional to the probability of radiative electron-hole recombination, and  $A$  is proportional to the defect density within the QW, and  $C$  to the probability of Auger recombination involving three carriers. It should be clear from Eq. 5.3.2 that, since the non-radiative term is linear in  $n$  and the radiative is quadratic in  $n$ , increasing the carrier concentration will increase the IQE of the system. I will demonstrate throughout the following two chapters that the image charge effect produces an increase in the IQE by producing strongly increased carrier concentrations in the vicinity of the NPs. For purposes of our modeling, I neglect the Auger recombination term as the term  $C$  is of the order  $10^{-30}$  in InGaN [63], which means Auger recombination plays no significant role at carrier concentrations of  $10^{18} \text{ cm}^{-3}$  and below.

In the case of plasmonics, IQE is increased by the addition of a second radiative recombination path provided by coupling to the SPs. This contribution of this new path becomes significant when the energy of emission of the QW matches the resonant energy of the SPs present. This enhancement occurs due to an increase in the rate of spontaneous e-h recombination [6, 7, 57] due to the Purcell effect [5].

The carriers in the QW, however, interact with the metal NPs not only through the evanescent SP fields but also via long-range Coulomb forces. When carriers are excited in the QW by an incident photon, the excited carriers are no longer electrically neutral. When excited near a metallic NP, the electric field produced by the carriers must induce a polarization in the NP which can be modeled for simple geometries as a charge distribution of equal and opposite magnitude within the metal. Since the induced charge

is always opposite that of the carrier, there will be an attractive force felt by the carrier. Coulomb attraction of carriers to the metallic NP causes them to drift towards the NP and thus increases the local concentration of e-h pairs, which results in an increase in the IQE and PL intensity adjacent to the NP. This universal electrostatic mechanism is unrestricted by frequency matching conditions such as those imposed on SP coupling, and therefore provides a means of enhancement for the efficiency of solid-state emitters over a wide range of frequencies.

#### 5.4 Modeling the Image Charge Effect

I demonstrate this effect by modeling the interaction of carriers in the vicinity of the nanoparticle using a simple drift/diffusion model of carrier transport. The partial differential equation defining the model takes the form:

$$\begin{aligned}\frac{\partial n}{\partial t} &= G_n - R_n + \frac{1}{e} \nabla \cdot \mathbf{J}_n \\ \frac{\partial p}{\partial t} &= G_p - R_p - \frac{1}{e} \nabla \cdot \mathbf{J}_p\end{aligned}\tag{5.4.1}$$

Here  $n$  represents the carrier concentration,  $G_n$  the rate of generation of new carriers, and  $R_n$  the rate of recombination. The term  $\mathbf{J}_n$  represents the movement of carriers within the system and can be replaced with the well-known carrier transport equation:

$$\begin{aligned}\mathbf{J}_n &= e\mu_n n \mathbf{E} + eD_n \nabla n \\ \mathbf{J}_p &= e\mu_p p \mathbf{E} - eD_p \nabla p\end{aligned}\tag{5.4.2}$$

Here  $e$  represents the elementary charge,  $\mu_n$  represents the mobility of the carriers,  $D_n$  the diffusion coefficient of the carriers, and  $\mathbf{E}$  an electric field present within the QW.

When inserted into Eq. 5.4.2 the first term of the carrier transport equations represents the drift of carriers due to the presence of an external electric field, and the second represents the diffusion of carriers from regions of high concentration towards regions of lower concentration. Substituting in Eq. 5.4.2 into Eq. 5.4.1 and replacing  $R$  with the total recombination rate from Eq. 5.3.2 gives us:

$$\begin{aligned}\frac{\partial n}{\partial t} &= D_n \nabla^2 n + \frac{e D_n}{k_B T} \nabla \cdot (n \mathbf{E}) - A n - B n p + G_n \\ \frac{\partial p}{\partial t} &= D_p \nabla^2 p + \frac{e D_p}{k_B T} \nabla \cdot (p \mathbf{E}) - A p - B n p + G_p\end{aligned}\tag{5.4.3}$$

Note that we have also rewritten the mobility  $\mu_n$  in terms of the diffusion coefficient using the Einstein relation  $D_n = \mu_n k_B T / e$ . In addition, we have used the radiative recombination rate in its proper form  $Bnp$ , as the recombination rate is proportional to the product of the carrier concentrations [62].

This set of coupled second-order non-linear partial differential equation (PDE) describes the motion of carriers within the quantum well in the presence of an electric field  $\mathbf{E}$ , which in our system represents the electric field of the induced image charge, and neglecting for the moment the geometry of the NP, essentially goes as  $-e/4r^2$ , where  $r$  is the distance of the carrier from the NP. In order to simplify the problem, we assume that  $n \cong p$ , which yields the following time-dependent PDE:

$$\frac{\partial p}{\partial t} = D_p \nabla^2 p + \frac{e D_p}{k_B T} \nabla \cdot (p E \hat{r}) - A p - B p^2 + G_p \quad (5.4.4)$$

For the reference system, the electric field in the drift term is  $E=0$ , and it is  $E=-e/4r^2$  for the NP system. In addition, I have used the following parameters for the material-dependent parameters  $A$ ,  $B$  [63] and  $D_p$  [11]:  $A = 6 \times 10^7 \text{ s}^{-1}$ ,  $B = 1 \times 10^{-10} \text{ cm}^3 \text{ s}^{-1}$ ,  $D = 12.5 \text{ cm}^2 \text{ s}^{-1}$ . In order to model a CW excitation, we take the generation term to be  $G_p = 1 \times 10^{16} \text{ cm}^{-3} \text{ s}^{-1}$  and set  $\partial p / \partial t = 0$  in Eq. 5.4.4. Figure 5.3 shows the carrier concentration for the steady-state solution with the given parameters at a variety of temperatures from 11K to 300K. It is clear from this plot that the carrier concentration diverges as  $r$  approaches the surface of the nanoparticles. Furthermore, as the temperature increases, the effective enhancement decreases by almost four orders-of-magnitude, significantly decreasing the enhancement provided by each NP. The second plot in Figure 5.3 shows the projected enhancement in the PL intensity as a function of temperature. I have calculated the far-field PL intensity as a function of time by

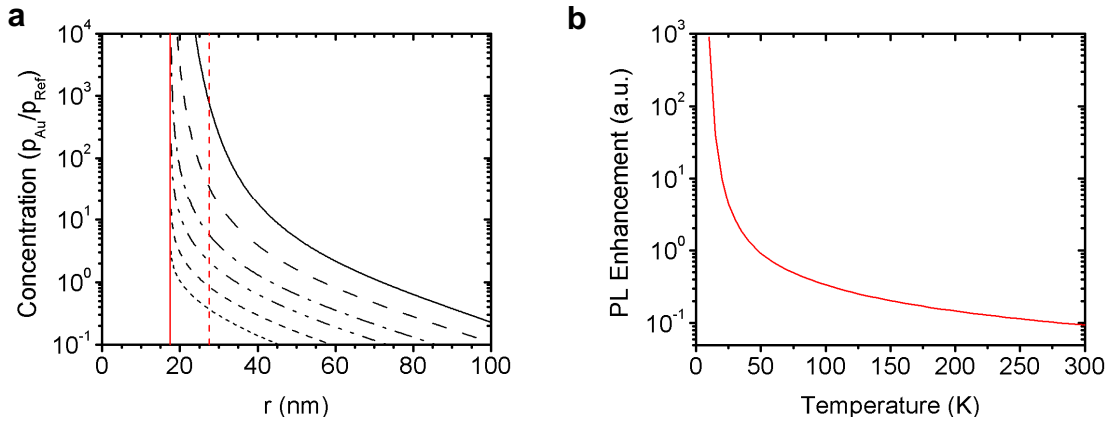


Figure 5.3 a, The carrier concentration as a function of distance from the Au NP in the steady-state model at temperatures from 11K to 300K. The solid red line represents the edge of the NP, and the dashed red line represents the nearest the carriers can approach the NP in the InGaN QW. b, PL Enhancement as a function of temperature in the steady-state model. Enhancement is calculated as the ratio of the Au NP Intensity to the reference intensity.

integrating the radiative recombination term over all space:

$$I(t) = \int_{r_0}^{\infty} Bp^2(r, t) dr \quad (5.4.5)$$

The enhancement in PL intensity is then defined as  $I_{Au}(t)/I_{Ref}(t)$ , the ratio of the emission intensity in the Au system to that of the reference.

In order to investigate the time-dependent properties of the system, we keep Eq. 5.4.4 as is, and take the generation term to be an instantaneous Gaussian excitation pulse equal to  $G_p = 1 \times 10^{16} \exp(-(r-r_0)^2/d) \delta(t)$ , where  $\delta(t)$  is the Dirac Delta function. Figure 5.4 shows the time evolution of the carrier concentration for both systems. Figure 5.5 shows the PL Intensity as a function of time for both the reference and Au NP systems. It is important to point out that our model has qualitatively similar behavior to the time-resolved photoluminescence measurements presented in Figure 5.2. The origin of the slower decay in the Au NP sample becomes clear when the curves are fitted using a three component exponential of the form:

$$I(t) = A_{NR}e^{-t/\tau_{NR}} + A_R e^{-t/\tau_R} + A_{Err}e^{-t/\tau_{Err}} \quad (5.4.6)$$

Here the first two exponentials represent the non-radiative and radiative decay components respectively, and the third term represents error introduced due to the finite size of the computational domain\*. Table 5.1 shows the results of this exponential fit.

---

\* Because of the finite size of the domain of calculation, carriers that diffuse out of the domain are lost. This loss of carriers from the domain shows up as a third decay component in the intensity.

Table 5.1 Decay constants and ratio of amplitudes of the radiative to non-radiative components of decay.

	$\tau_{NR}$ (ns)	$\tau_R$ (ns)	$\tau_{Err}$ (ns)	$A_R/A_{NR}$
Ref	0.149	0.616	2.73	0.428
Au	0.151	0.609	3.06	0.738

It turns out that the lifetimes in the two systems are essentially unchanged. Instead the decreased rate of decay occurs due to a change in the ratio of radiative to non-radiative recombination. This change in ratio is evidence of the increase in IQE due to the presence of the Au NP.

## 5.5 Power Saturation and Screening

In our model, I have assumed that carriers are able to be attracted to their image charges, and neglected any interactions between the carriers. While scattering and other many-body interactions are likely to play a role in carrier dynamics in the high

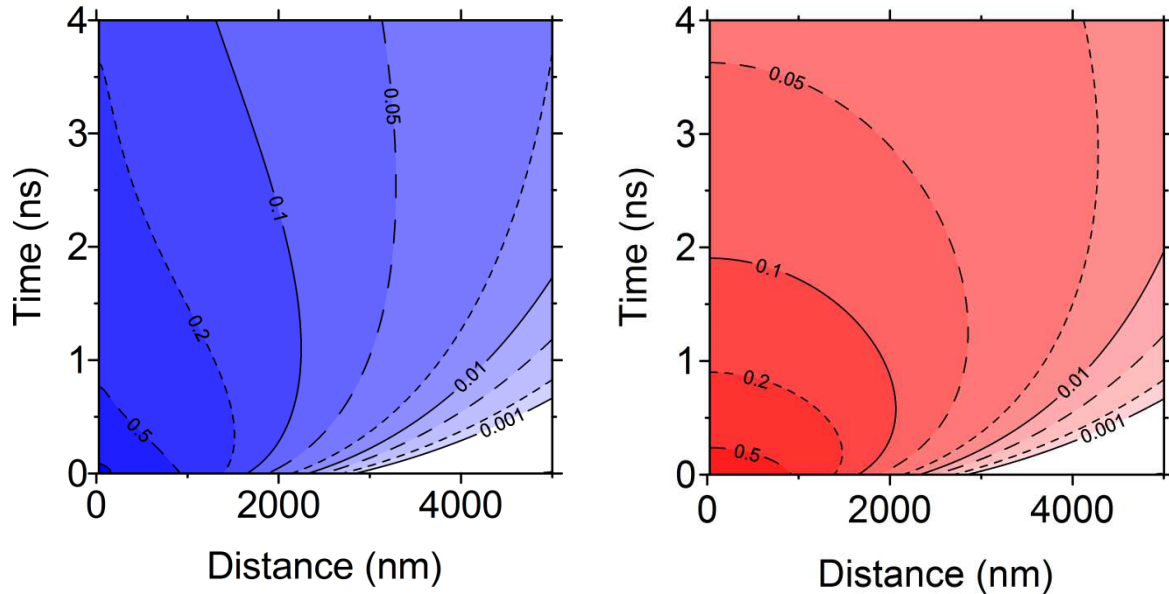


Figure 5.4 a, The carrier concentration as a function of time for the Au NP system. b, The same for the reference system. In both plots the concentration has been normalized so that  $\rho(\delta,0)=1$ .

concentration region near the NP, the primary many-body effect that has been neglected in this model is that of electrostatic screening.

In a semiconductor heterostructure, the excited carriers take the form of a neutral plasma. Within a semiconductor plasma, the Coulomb interactions are screened off by free carriers causing the electric field to decay faster than  $r^{-2}$ . The distance over which an electrostatic charge is screened by free carriers in a semiconductor is given by the Debye radius:

$$r_D(t) = \sqrt{\frac{\epsilon_r \epsilon_0 k_B T}{q^2 2 p(t)}} \quad (5.5.1)$$

Since  $r_D \propto \sqrt{T/p}$  the strength of attraction due to the image charge effect is decreased due to screening at higher pumping powers when more e-h pairs are created. This should result in a power-dependent saturation in the PL intensity.

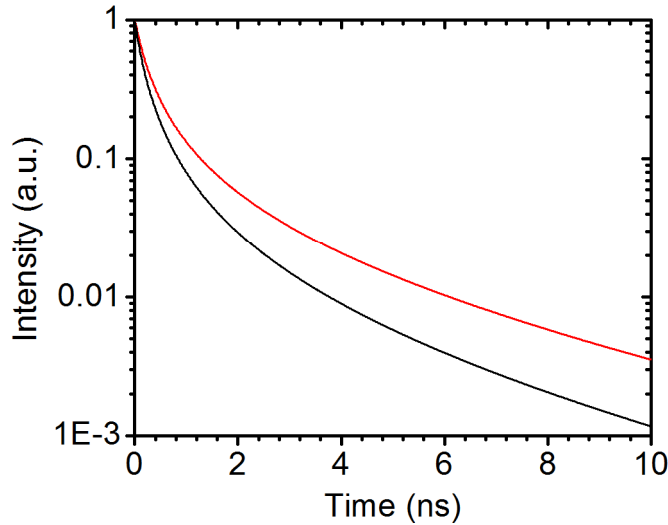


Figure 5.5 PL Intensity calculated using Eq. 5.4.5 for the Au NP (Red) and reference (Black) systems as a function of time after excitation by an instantaneous Gaussian pulse. Note that the decay of the Au NP system is slower overall than that of the reference.

Experimental evidence of this power-dependent saturation is presented in Figure 5.7. For the InGaN QW at 11K at low power densities ( $\sim 0.1 \text{ mW cm}^{-2}$ ) the Debye radius is about 50 nm, i.e. the screening does not affect much the forces attracting the carriers to the sphere. Screening, however, becomes relevant at the

powers densities exceeding  $3 \text{ mW cm}^{-2}$  when the Debye radius becomes smaller than the typical size of the nanospheres. Figure 5.6 shows the Debye radius as a function of elapsed time and excitation power density for the reference sample. We note that our calculations for the Debye radius presented here underestimate the actual value of  $r_D$  due to the assumption that the rate of conversion of incident photons to carriers in the QWs is unity.

It is also clear that the Debye radius decreases with decreasing temperature. This dependence explains the lower overall gain in IQE and PL enhancement for the Au NP sample as compared to the reference sample at lower temperatures in the CW PL experiment. This decrease in the radius reduces the area of increased concentration surrounding the NP, and hence lowers the effective carrier concentration. The Debye radius, however, decreases as  $T^{1/2}$ , while the strength of the image charge effect

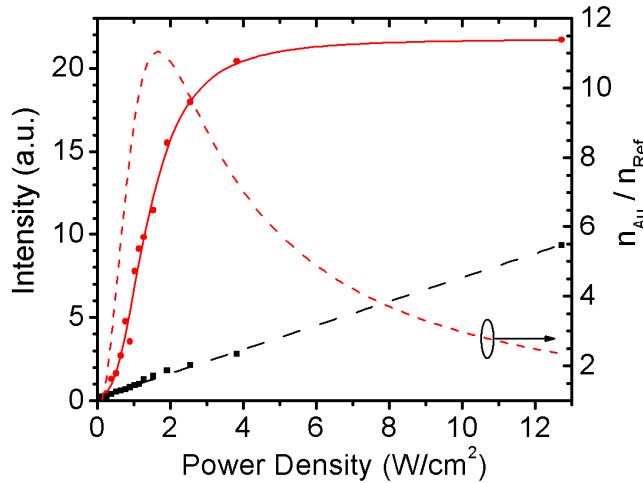


Figure 5.7 PL Intensity as a function of incident power density for the Au (red circles) and reference (black squares) systems. The dashed red line represents the effective carrier concentration of the Au system in units of the reference concentration.

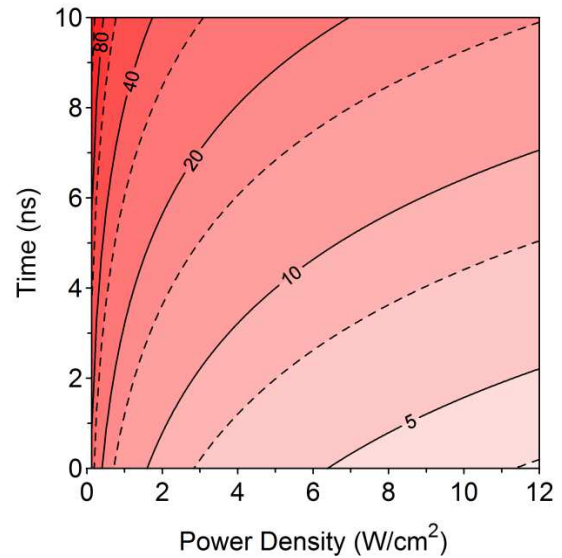


Figure 5.6 Debye radius (nm) as a function of time and excitation power density for the reference system.



increases as  $1/T$ , so one still can still expect the overall enhancement to grow as the temperature drops.

I address here also the attraction of electron-hole pairs towards the nanoparticles within the QW. While it is clear that a single hole or electron will be attracted to a nanoparticle, it is not intuitively obvious that an electron-hole pair will experience a similar attraction. Instead one might expect that the primary interaction between the e-h pair and its image would be a dipole-dipole in nature which would produce a negligible attraction. To investigate this problem I solved for the acceleration of the center-of-mass of the e-h pair for a variety of orientations and distances from the NP surface. For simplicity I take the separation between the electron and hole to be equal to the exciton Bohr radius in InGaN,  $\sim 3\text{nm}$ . The net acceleration on the system is (see Appendix A)

$$a_{cm}(r, \theta) = -\frac{e^2}{4 \epsilon \mu} \left( \frac{1}{\left(d + \frac{\mu}{m_e} r_{ex} \sin(\theta)\right)^2} + \frac{1}{\left(d - \frac{\mu}{m_h} r_{ex} \sin(\theta)\right)^2} - \frac{8 \left(2d + \frac{m_h - m_e}{m_h + m_e} r_{ex} \sin(\theta)\right)}{\left(r_{ex}^2 \cos^2(\theta) + \left(2d + \frac{m_h - m_e}{m_h + m_e} r_{ex} \sin(\theta)\right)^2\right)^{3/2}} \right) \quad (5.5.2)$$

where  $r_{ex}$  is the separation between the electron and hole,  $d$  the distance to the surface of the NP,  $m_{e,h}$  the masses of the electron and hole,  $\mu = m_e m_h / (m_e + m_h)$  (i.e. the reduced mass of the e-h pair), and  $\theta$  the orientation of the pair with respect to the surface. Figure 5.8 presents a schematic of the system used for calculations and the results of the

calculations. . Note that there are some orientations with a net repulsion of the exciton for  $\theta < 0$  (i.e. the electron closer than the hole to the surface). However, in this case the effect of the forces is significantly weaker than the attraction experienced for the opposite orientation. This asymmetry arises from the differences in the effective mass of the two carriers within the QW.

Let us assume, for a moment, that all excitons were oriented with  $\theta < 0$ . In this case excitons would feel an attraction or repulsion based upon their distance from the surface. For distances less than the critical distance  $D \approx 30$  nm, the attraction ranges from 1 to 3 orders-of-magnitude larger than the repulsive force felt at  $d > D$ . This huge attraction near to the surface results in a significant gradient in the carrier concentration as it depletes the carriers in the region around 25-30nm. This gradient, in turn, results in an inward diffusion that would easily negate the weak repulsion experienced by the excitons beyond the critical distance.

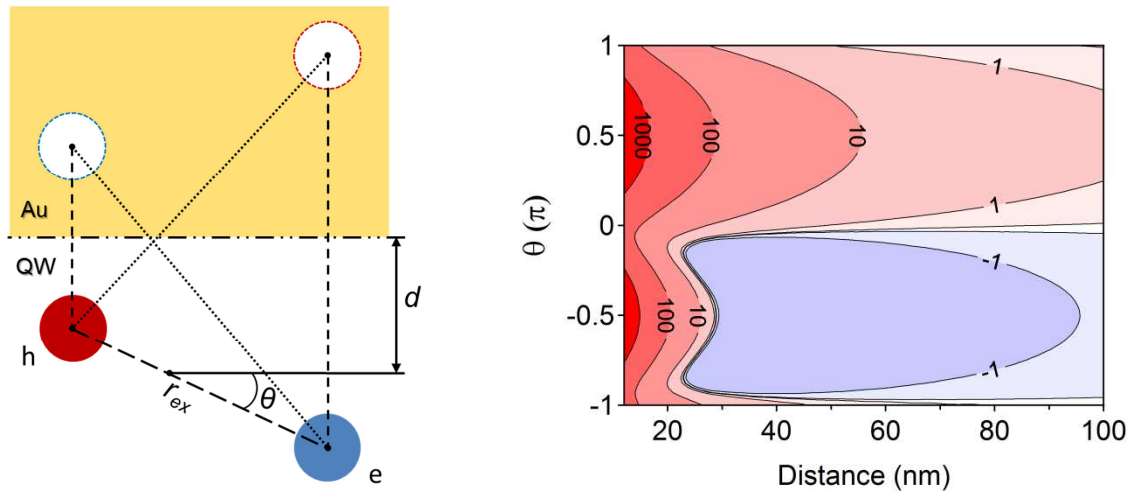


Figure 5.8 a, Schematic diagram of the electron-hole pair and its image used for computing the net acceleration of the e-h pair. b, Net acceleration on an e-h pair with orientation  $\theta$  and distance  $d$  from the surface of the nanoparticle. Red represents a net acceleration towards the NP, and blue away from it. Each contour represents an order of magnitude change in the respective direction.

If we now include the fact that the exciton orientations are randomly distributed, we find that carriers with  $\theta > 0$  will be strongly attracted at significantly further distances than for those with  $\theta < 0$ . This means that even if the diffusion mentioned before were insufficient to negate the weak repulsion experienced by those excitons, there would still be a net migration inward as carriers with  $\theta > 0$  are pulled in from further out and attracted more effectively than the others are repelled. Thus one must conclude that the image charge effect produces a net attraction for carriers even when accounting for dipole-dipole interactions instead of the Coulomb attraction experienced by individual carriers. I also note that attractive forces have been predicted for excitons in CdS nanorods interacting with images induced in Au nanoparticles attached to the end of the nanorod. [64].

## 5.6 Angle Dependent PL measurements

One of the consequences of the image charge effect as applied to dipoles is that the maximum acceleration for the e-h pairs occurs when the pair is oriented normal to the NP. This makes sense from a minimization of energy standpoint, as the energy of a system of two dipoles is minimized when the two are aligned in the same direction. This suggests that a majority of carriers in the vicinity of NPs should be oriented normal to the surface. Any change in the distribution of carrier orientations should produce a change in the angular distribution of emitted photons. In order to investigate this, the samples were subjected to angle-dependent PL measurements, the results of which are presented in Figure 5.9. Since the emission is travelling from a high-index material ( $n_{\text{GaN}} \cong 2.5$ ) to a lower index material ( $n_{\text{Air}}=1$ ) I have normalized the emission intensities to account for the transmission as a function of angle (see Appendix B). I present both the

integrated PL intensity as well as the peak PL intensity to highlight a disparity which arises between the two. The integrated intensities show little variation with angle prior to 60°, with the Au showing an overall enhancement and the Ag sample a reduction in intensity. The peak intensities, however, tell a different story. In this case the angle at which the peak intensity is reached varies significantly between the three samples. While reference sample peaks at 35°, the Ag NP sample peaks 5° earlier at 30°, and the Au NP sample 10° later.

If this change in angle were due to scattering by the NPs, one would expect to see both the integrated and peak intensities showing a peak at the same angle. Furthermore, the same would be expected if the change in peak intensity were entirely due to a change in the distribution of carrier orientations within the QW due to the aforementioned minimization of energy near the NPs. Instead the disparity between the

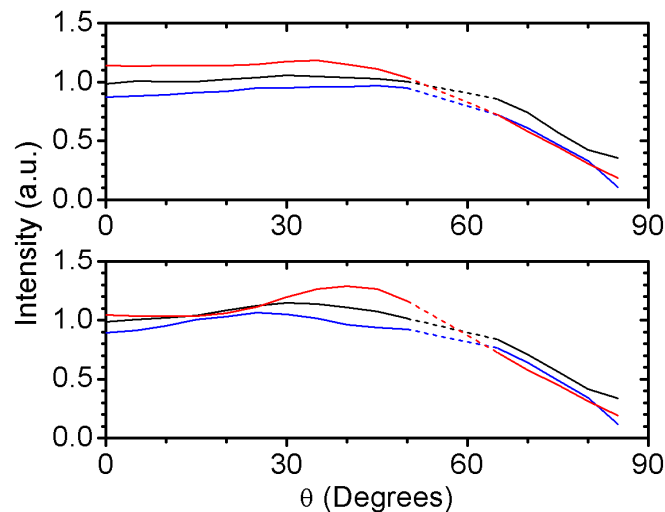


Figure 5.9 a, The peak PL intensity as a function of the measurement angle  $\theta$  for the reference (black), Au NP (red) and Ag NP (blue) samples. b, The integrated PL intensity as a function of the measurement angle. In both a and b the intensities are normalized to that of the reference sample at 0° and to the transmission as a function of angle. The dashed segment of the line represents linear interpolation of missing data points.

two PL measurements suggests that, while the total number of photons is essentially constant with angle prior to 60°, at angles away from the maximum there is some form of broadening of the PL spectrum. In fact, if we fit the PL spectra using the fitting method discussed in §3.7, we see that there is an exchange in emission between the main emission of the quantum well and the first and second phonon-replicas of the peak.

### 5.7 Modification of Electron-Phonon Coupling

The origin of phonon replicas, as explained in §2.5 is due to electron phonon coupling within the QW. Interaction between electrons and the lattice produces a non-zero probability of emitting a phonon during recombination. It is well known that the strength of the electron-phonon coupling is a function of the wavevector of the phonon as well as the orientation of the exciton. Since we know that the presence of the NPs

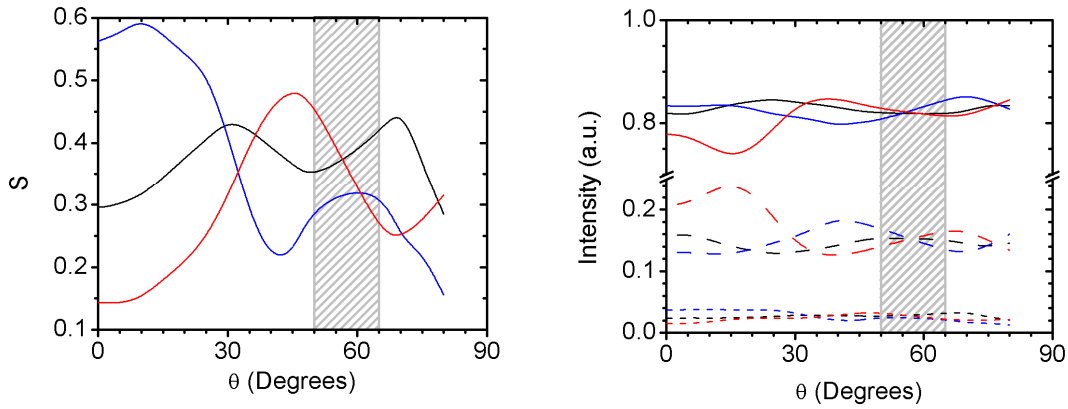


Figure 5.10 a, The Huang-Rhys parameter  $S$  as a function of angle for the reference (black), Au NP (red) and Ag NP (blue) samples. b, The intensity of the main emission and first (dashed) and second (dotted) phonon replicas normalized with respect to the total emission (i.e.  $I_{PR-0} + I_{PR-1} + I_{PR-2} = 1$ ). The gray shaded region represents missing values replaced by interpolation with a spline.

must produce some change in the distribution of carriers within the QW, we expect that the image charge effect must alter the probability of recombination producing phonons, and hence alter the intensity of the phonon replicas.

Figure 5.10 shows the Huang-Rhys parameter  $S$  as well as the intensity of the main emission and its two phonon replicas. It is clear that there is significant exchange of emission intensity in the Au NP sample to the primary emission from the first phonon replica between 15 and 35°. This switch lines up with a significant change in the value of  $S$  from 0.15 to ~0.5. This contrasts strongly with both the reference system, which has a smaller overall change in  $S$ , and experiences less exchange in emission between peaks, and the Ag sample, whose behavior seems to be the antithesis of the Au NP

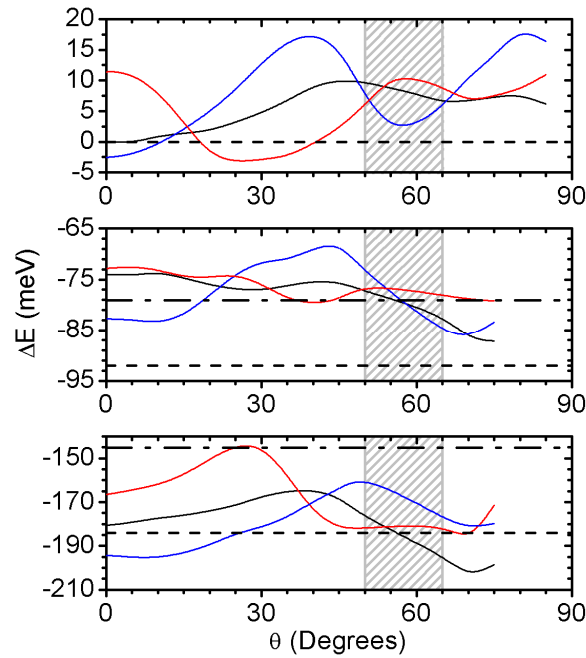


Figure 5.11 a, Emission energy of the main emission for reference (black), Ag (blue) and Au (red) measured as a deviation from the reference emission energy of 2.984 eV. b, Emission energy of the first phonon-replica. c, Emission energy of the second phonon replica. The black dashed lines represent the uncorrected energies of the three peaks. The black dot-dashed lines represent the energies of the phonon replicas corrected for their temperature dependence. The gray shaded region represents missing values replaced by interpolation with a spline.

sample.

I have also measured the energy of the primary emission and the phonon replicas. As discussed previously, in InGaN the phonon replicas are separated from the main peak by the energy of one or more LO phonons ( $\hbar\omega_{LO}=92$  meV). Since the distribution of phonons is not Gaussian, the peak of the first and second phonon replicas are offset from their expected positions by  $1/2$  and  $3/2$   $kT$  respectively, where  $kT \sim 26$  meV at room temperature. Figure 5.11 shows the energies of the three peaks measured as meV deviations from the reference emission energy of 2.984 eV. While I am unsure of the origin of the discrepancy, it is interesting to note that the first phonon replica energies line up well with the corrected phonon replica energy whereas the second phonon replica lines up more closely with the uncorrected values.

## 5.8 Near-field Spectroscopy

It is clear from the simulations that the image charge effect should produce a

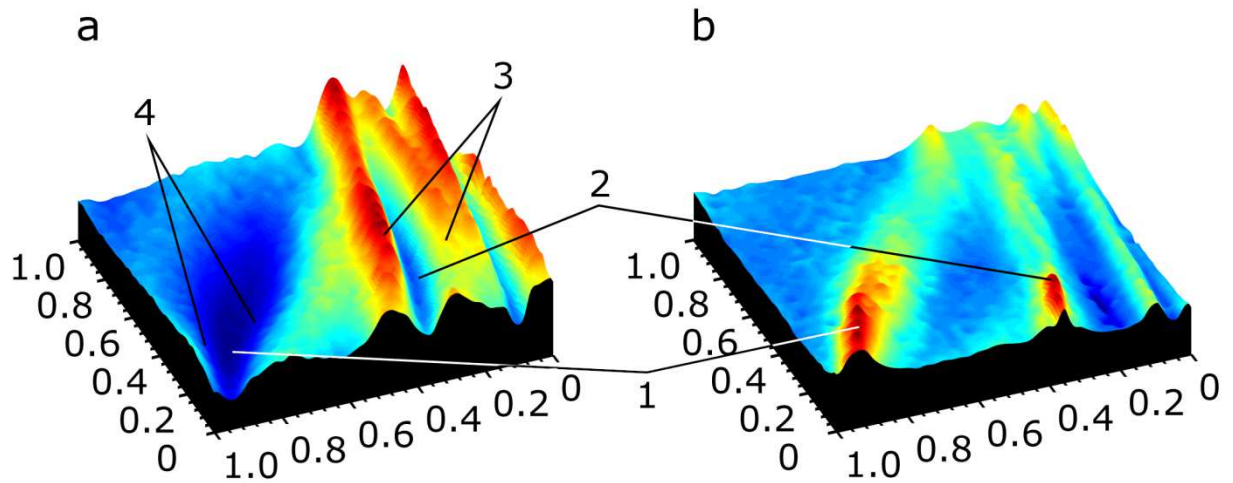


Figure 5.12 a, Map of the integrated near-field PL intensity in a 1x1 micron region of the Au NP sample. b, Map of the PL intensity of the QWs within the pits in the same region. Note that the intensity of the regions immediately surrounding the pits at 1 and 2 differ significantly. The pits at 2 show significant emission in the adjacent region 3, whereas the pits at 2 show weak emission intensity in the surrounding region 4.

strongly inhomogeneous distribution of light emission in a small region around the nanoparticle. Since the regions over which this intensity variation occurs are smaller than  $\lambda/2$ , it is not possible to resolve the inhomogeneity in emission near the NP using far-field PL measurements. Instead, I have used near-field spectroscopy, which is capable of resolving sub-wavelength features on the order of the width of the probe aperture used for the measurements (see §3.6). Ideally, near-field measurements would be done using an AFM-type NSOM instead of a fiber-probe based NSOM, which would allow for topographical mapping of the individual pits to correlate pit positions with the emission intensity. In the absence of this I make use of the fitting method used for near-field measurement of InGaN/GaN samples which allows us to measure emission from the QWs within the pits themselves.

We present the results of a near-field measurement showing enhancement from Au NPs in Figure 5.12. The imaged 1x1 micron region has two areas of pits, one of which shows significantly enhanced emission in the vicinity of the pits. An increase in

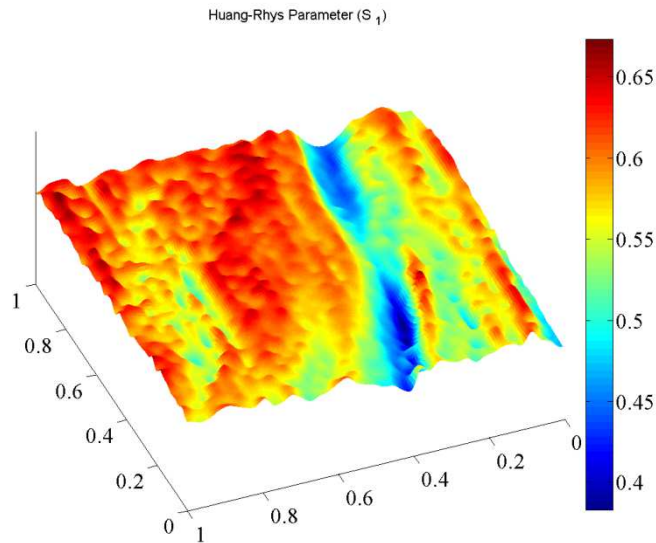


Figure 5.13 Huang-Rhys Parameter extracted via fitting the same 1x1 micron area depicted in Fig 5.12



near-field PL intensity and the presence of pits, however, are not sufficient to prove the region is enhanced by the presence of Au NPs. In fact it is widely known that there can be significant inhomogeneities in emission intensity and energy in InGaN quantum wells [65-67]. One way of proving the presence of NPs is to correlate the spectral features of the emission near the NP to those observed in the far-field. Specifically it is known that there are strong changes in the strength of the electron-phonon coupling in the vicinity of the Au NPs. Figure 5.13 shows the value of the Huang-Rhys parameter in the same 1x1 micron area imaged in Figure 5.12. This map is derived using the same fitting algorithm used in the angle dependent measurements. It is clear that the area depicted in Figure 5.12 region 3 has a much smaller value of  $S$  than that of Region 4. This correlates well with the overall lower value of  $S$  for the Au NP sample when compared with the reference, and hence suggests strongly that the emission near the pits is due to the nanoparticles.

## 5.9 Fluorescence Lifetime Imaging Microscopy

In order to clearly demonstrate the inhomogeneity of the lifetime and PL on a small scale, I have made use of Fluorescence Lifetime Imaging Microscopy (FLIM) to map the decay constant and intensity over a large region of the sample with ~300nm resolution. Figure 5.14 demonstrates a clear difference between the homogeneity of emission in the reference sample (panel c) and that of the Au NP sample (panel a). Furthermore, the decay constants measured for the Au NP sample (panel b) show a strong positive correlation between lifetime and intensity, whereas the decay constants for the reference sample show no correlation with intensity at all. This inhomogeneity in

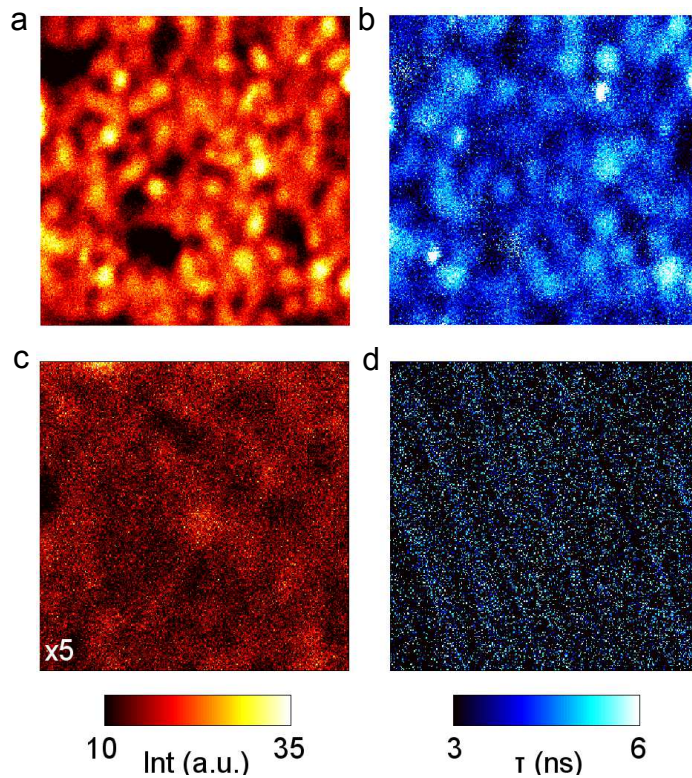


Figure 5.14 FLIM imaging of a 10x10 micron region of the Au NP sample showing the (a) intensity and (b) decay constant of the sample. Note the strong correlation between emission intensity and the measured decay constant. The reference sample intensity (c) over a region of the same size shows a significantly homogenized emission, and the (d) lifetime shows no correlation with the emission intensity.

intensity and decay constant are exactly what is predicted by the model presented here for the image charge effect.

## 5.10 Summary and Future Research

Clearly the results presented here demonstrate the existence of a non-resonant mechanism of emission enhancement which arises from the interaction of carriers with their image charges within a neutral metal. This interaction results in strongly localized light emission, increased IQE and recombination lifetimes, and power-dependent saturation of the

emission intensity. Due to its non-resonant nature, the image charge effect provides a means of enhancing optical emission in light-emitting devices where the precise tailoring of energies required for resonant enhancement is difficult. Furthermore, the image charge effect provides an opportunity to tailor two features of systems which, to our knowledge, have not been able to be controlled on the nanoscale externally. Firstly the inhomogeneous carrier concentrations produced by the mechanism open the door to tailoring carrier concentrations within nanoscale regions and localizing light emission,

something which has only been considered for plasmonic devices to date [68, 69]. Secondly, the changes in the electron-phonon coupling strength hint at the possibility of tailoring electron-phonon interactions in the vicinity of metallic NPs using the image charge effect.

Furthermore, while both plasmonics and the image charge effect have a similar end result -- enhancement -- they have different physical origins. Since the two mechanisms arise in similar situations, it is important to make the following points: First, it is likely possible to tailor systems in which both plasmonics and the image charge effect simultaneously manifest. In these situations both constructive and destructive interactions between the two may arise. Our own Ag system provides evidence of the possibility of destructive competition between the two. Recently, anomalously large enhancements have been reported in In/InN [70] and Ag/ZnO systems [71]. Since the system used is favorable for strong image charge interaction, I hypothesize that this system provides evidence of constructive interaction between plasmonics and the image charge effect. Any complete understanding these systems must consider the possibility of these interactions. Second, care should be taken separate out the effects of each mechanism in experiments or devices designed to make use of either, i.e. some effects, including emission enhancement, which are currently attributed to plasmonics could instead arise due to the image charge effect. An example of this would be the attribution to plasmonics of enhancement in systems which should be non-resonant. For example, the plasmonic mechanism has been invoked to explain enhancement of UV emission in a Au/ZnO system [72] as well as nano-patterned Pt thin films [73]. Since the

the plasmon energies for Au and Pt are well below the emission energy of ZnO, enhancement due to coupling to plasmons should be ruled out

While I have done considerable work to demonstrate this effect, much work remains to be done. Specifically, as mentioned above, more work needs to be done to understand the interactions between the image charge effect and plasmons. A full understanding should be able to explain the decrease in intensity of the Ag NP system as well as possible situations in which constructive cooperation can occur between the two mechanisms. Additionally, a significant amount of work needs to be done in order to provide a model which accurately describes both the angle dependent measurements as well as the changes to the electron-phonon coupling due to the image charge effect. I plan on further investigating these effects both experimentally and theoretically via a variety of techniques. From an applications standpoint, investigating the electronic properties of the image charge effect is essential. Techniques such as cathodoluminescence, photocurrent and electroluminescence measurements as well as C-V and I-V measurements would go a long way towards providing an understanding of the image charge effect in an electronic context.

APPENDIX A

DERIVATION OF EQUATION FOR NET FORCE ON EXCITON

Let us begin by defining the position vectors for the electron ( $\mathbf{r}_e$ ), the hole ( $\mathbf{r}_h$ ) and their images ( $\mathbf{r}_{ei}$ ,  $\mathbf{r}_{hi}$ ). The diagram in Figure A.1 shows the relationships of the various vectors we'll use in this derivation. We define the position of the electron and hole in terms of the center of mass of the electron-hole pair as such:

$$\begin{aligned}\mathbf{r}_e &= \mathbf{r}_{cm} + \mathbf{r}_- \\ \mathbf{r}_h &= \mathbf{r}_{cm} - \mathbf{r}_+\end{aligned}\tag{A.1}$$

Here  $\mathbf{r}_{cm}$  is the vector describing the position of the center of mass and  $\mathbf{r}_-$  and  $\mathbf{r}_+$  the relative positions of the electron and hole.

Next we note that the relationship between the position vectors of the electron and hole and their images are related by a mirror transformation across the x-axis. This transformation leaves the x-component of the vector untouched and inverts the z-

component. We will write the transformation as such:

$$\mathbf{r}' = \mathbf{r} \cdot (\hat{x}\hat{x} - \hat{z}\hat{z})\tag{A.2}$$

At this point we will also define the identity transformation for future use:

$$\mathbf{r}' = \mathbf{r} \cdot (\hat{x}\hat{x} + \hat{z}\hat{z}) = \mathbf{r}\tag{A.3}$$

Using the mirror transformation given by Eq. (A2.2) we can now define the vectors which describe the positions of the electron and hole images as such:

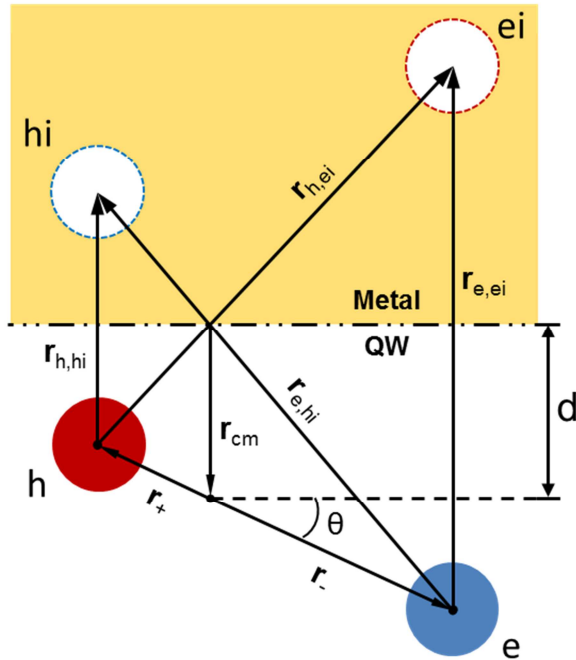


Figure A.1 Schematic Diagram of the exciton used for this derivation.

$$\begin{aligned}
\mathbf{r}_{ei} &= \mathbf{r}_e \cdot (\hat{\mathbf{x}}\hat{\mathbf{x}} - \hat{\mathbf{z}}\hat{\mathbf{z}}) = (\mathbf{r}_{\text{cm}} + \mathbf{r}_-) \cdot (\hat{\mathbf{x}}\hat{\mathbf{x}} - \hat{\mathbf{z}}\hat{\mathbf{z}}) \\
\mathbf{r}_{hi} &= \mathbf{r}_h \cdot (\hat{\mathbf{x}}\hat{\mathbf{x}} - \hat{\mathbf{z}}\hat{\mathbf{z}}) = (\mathbf{r}_{\text{cm}} - \mathbf{r}_+) \cdot (\hat{\mathbf{x}}\hat{\mathbf{x}} - \hat{\mathbf{z}}\hat{\mathbf{z}})
\end{aligned} \tag{A.4}$$

From these four vectors ( $\mathbf{r}_e$ ,  $\mathbf{r}_h$ ,  $\mathbf{r}_{ei}$ ,  $\mathbf{r}_{hi}$ ) we can then define the vectors describing the distances between all the pairs of charges except the image charges, which cannot exert a force upon each other. In calculating the vectors between the real charges and their images, we will make use of the identity transformation to simplify notation.

$$\begin{aligned}
\mathbf{r}_{e,h} &= \mathbf{r}_e - \mathbf{r}_h = (\mathbf{r}_{\text{cm}} + \mathbf{r}_-) - (\mathbf{r}_{\text{cm}} - \mathbf{r}_+) \\
&= \mathbf{r}_- + \mathbf{r}_+ \equiv \mathbf{R}_+ \\
\mathbf{r}_{e,ei} &= \mathbf{r}_e - \mathbf{r}_{ei} \\
&= \mathbf{r}_e \cdot (\hat{\mathbf{x}}\hat{\mathbf{x}} + \hat{\mathbf{z}}\hat{\mathbf{z}}) - \mathbf{r}_e \cdot (\hat{\mathbf{x}}\hat{\mathbf{x}} - \hat{\mathbf{z}}\hat{\mathbf{z}}) \\
&= \mathbf{r}_e \cdot (\hat{\mathbf{x}}\hat{\mathbf{x}} + \hat{\mathbf{z}}\hat{\mathbf{z}} - \hat{\mathbf{x}}\hat{\mathbf{x}} + \hat{\mathbf{z}}\hat{\mathbf{z}}) \\
&= 2 \mathbf{r}_e \cdot \hat{\mathbf{z}}\hat{\mathbf{z}} \\
\mathbf{r}_{e,hi} &= \mathbf{r}_e - \mathbf{r}_{hi} \\
&= \mathbf{r}_e \cdot (\hat{\mathbf{x}}\hat{\mathbf{x}} + \hat{\mathbf{z}}\hat{\mathbf{z}}) - \mathbf{r}_h \cdot (\hat{\mathbf{x}}\hat{\mathbf{x}} - \hat{\mathbf{z}}\hat{\mathbf{z}}) \\
&= (\mathbf{r}_e - \mathbf{r}_h) \cdot \hat{\mathbf{x}}\hat{\mathbf{x}} + (\mathbf{r}_e + \mathbf{r}_h) \cdot \hat{\mathbf{z}}\hat{\mathbf{z}} \\
&= \mathbf{R}_+ \cdot \hat{\mathbf{x}}\hat{\mathbf{x}} + (2 \mathbf{r}_{\text{cm}} + \mathbf{r}_- - \mathbf{r}_+) \cdot \hat{\mathbf{z}}\hat{\mathbf{z}} \\
&= \mathbf{R}_+ \cdot \hat{\mathbf{x}}\hat{\mathbf{x}} + (2 \mathbf{r}_{\text{cm}} + \mathbf{R}_-) \cdot \hat{\mathbf{z}}\hat{\mathbf{z}}
\end{aligned} \tag{A.5}$$

The remaining two vectors ( $\mathbf{r}_{h,hi}$ ,  $\mathbf{r}_{h,ei}$ ) can be obtained from those for the electron by letting  $e \rightarrow h$  and  $\hat{\mathbf{x}}\hat{\mathbf{x}} \rightarrow -\hat{\mathbf{x}}\hat{\mathbf{x}}$ . For convenience we have defined  $\mathbf{R}_+$  and  $\mathbf{R}_-$  to represent the quantities  $(\mathbf{r}_- + \mathbf{r}_+)$  and  $(\mathbf{r}_- - \mathbf{r}_+)$  respectively.

The electric potential experienced by the electron is given by the the equation:

$$\begin{aligned}
\Phi_e &= \frac{e}{\epsilon} \left( \frac{1}{|\mathbf{r}_{e,h}|} + \frac{1}{|\mathbf{r}_{e,ei}|} - \frac{1}{|\mathbf{r}_{e,hi}|} \right) \\
&= \frac{e}{\epsilon} \left( \frac{1}{|\mathbf{R}_+|} + \frac{1}{|2\mathbf{r}_e \cdot \hat{\mathbf{z}}\hat{\mathbf{z}}|} - \frac{1}{|\mathbf{R}_+ \cdot \hat{\mathbf{x}}\hat{\mathbf{x}} + (2\mathbf{r}_{\text{cm}} + \mathbf{R}_-) \cdot \hat{\mathbf{z}}\hat{\mathbf{z}}|} \right) \\
&= \frac{e}{\epsilon} \left( \frac{1}{R_+} + \frac{1}{2\mathbf{r}_e \cdot \hat{\mathbf{z}}} - \frac{1}{\sqrt{(\mathbf{R}_+ \cdot \hat{\mathbf{x}})^2 + ((2\mathbf{r}_{\text{cm}} + \mathbf{R}_-) \cdot \hat{\mathbf{z}})^2}} \right)
\end{aligned} \tag{A.6}$$

The  $x(z)$  component of  $\mathbf{R}_{+,-}$  is given by  $R_{+,-}\cos(\theta)$  ( $R_{+,-}\sin(\theta)$ ). Furthermore, we assume that the center of mass of the electron-hole pair is  $\mathbf{r}_{\text{cm}} = d \hat{\mathbf{z}}$ . Making these substitutions into Eq. (A2.6) yields:

$$\begin{aligned}
\Phi_e &= \frac{e}{\epsilon} \left( \frac{1}{R_+} + \frac{1}{2\mathbf{r}_e \cdot \hat{\mathbf{z}}} - \frac{1}{\sqrt{(\mathbf{R}_+ \cdot \hat{\mathbf{x}})^2 + ((2\mathbf{r}_{\text{cm}} + \mathbf{R}_-) \cdot \hat{\mathbf{z}})^2}} \right) \\
&= \frac{e}{\epsilon} \left( \frac{1}{R_+} + \frac{1}{2(d + r_- \sin(\theta))} - \frac{1}{\sqrt{R_+^2 \cos^2(\theta) + (2d + R_- \sin(\theta))^2}} \right)
\end{aligned} \tag{A.7}$$

This time the potential experienced by the hole  $\Phi_h$  may be obtained by letting  $r_- \rightarrow -r_+$  and  $e \rightarrow -e$ .

The electric field, in turn, is simply the minus the gradient of the potential. Since we are interested specifically in the attraction towards the surface, we will only consider the  $z$ -component of the electric field here. For the electron we have:



$$\begin{aligned}
\mathbf{E}_e &= -\nabla\Phi_e = -\frac{\partial}{\partial z}\Phi_e\hat{\mathbf{z}} = -\frac{\partial d}{\partial z}\frac{\partial}{\partial d}\Phi_e\hat{\mathbf{z}} = -\frac{1}{2}\frac{\partial}{\partial d}\Phi_e\hat{\mathbf{z}} \\
&= -\frac{e}{4\epsilon}\left(\frac{1}{(d+r_-\sin(\theta))^2} - \frac{4(2d+R_-\sin(\theta))}{(R_+^2\cos^2(\theta) + (2d+R_-\sin(\theta))^2)^{3/2}}\right)\hat{\mathbf{z}} \quad (\text{A.8})
\end{aligned}$$

Due to the fact that  $z$  is the variable that defines the variation of the electric field, our gradient must be taken with respect to it. For our system, however,  $d$  determines the position along the  $z$ -axis of the e-h pair, so we need to convert our derivative from  $z$  to  $d$ . The ratio  $\partial d/\partial z = 1/2$  (derived from  $z=2d$ ) is the term that allows for this conversion. The same substitution used to get  $\Phi_h$  may be used again to get  $\mathbf{E}_h$ .

The net force acting on the center of mass of the e-h pair is just the sum over the forces acting on the electron and hole:

$$\begin{aligned}
\mathbf{F}_{ex} &= e\mathbf{E}_e - e\mathbf{E}_h \\
&= -\frac{e}{4\epsilon}\left(\frac{1}{(d+r_-\sin(\theta))^2} - \frac{4(2d+R_-\sin(\theta))}{(R_+^2\cos^2(\theta) + (2d+R_-\sin(\theta))^2)^{3/2}}\right)\hat{\mathbf{z}} \\
&\quad -\frac{e}{4\epsilon}\left(\frac{1}{(d-r_+\sin(\theta))^2} - \frac{4(2d+R_-\sin(\theta))}{(R_+^2\cos^2(\theta) + (2d+R_-\sin(\theta))^2)^{3/2}}\right)\hat{\mathbf{z}} \quad (\text{A.9}) \\
&= -\frac{e}{4\epsilon}\left(\frac{1}{(d+r_-\sin(\theta))^2} + \frac{1}{(d-r_+\sin(\theta))^2} \right. \\
&\quad \left. - \frac{8(2d+R_-\sin(\theta))}{(R_+^2\cos^2(\theta) + (2d+R_-\sin(\theta))^2)^{3/2}}\right)\hat{\mathbf{z}}
\end{aligned}$$

Finally we redefine  $r_{+,-}$  and  $R_{+,-}$  in terms of the separation between the electron and hole  $r_{ex}$ . It is immediately obvious that  $R_+ = r_- + r_+ = r_{ex}$ , furthermore it is well known that the lengths of the vectors relative to the center of mass for a two-mass

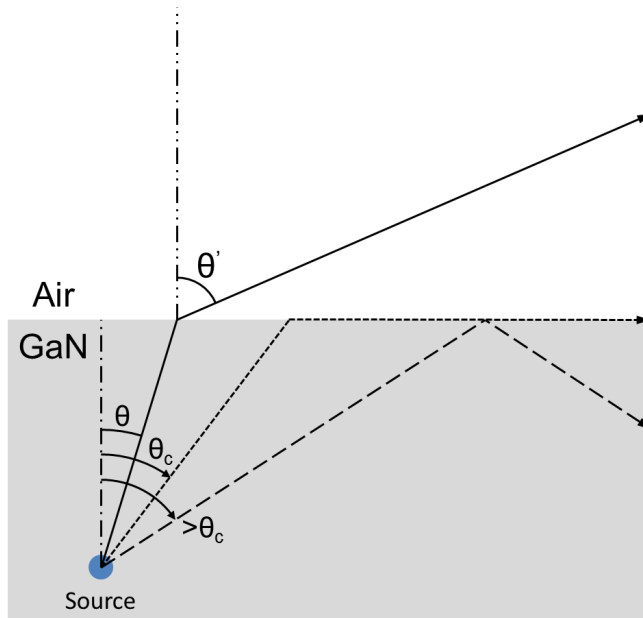
system can be defined by  $r_i = \mu r_{ex}/m_i$  where  $\mu$  is the reduced mass of the system. From this we can also determine that  $R_- = r_- - r_+ = ((m_e - m_h)/m_e m_h) \mu r_{ex} = ((m_e - m_h)/(m_e + m_h)) r_{ex}$ . Using these relations we get the final version of the force on the exciton:

$$\begin{aligned}
 \mathbf{F}_{ex} &= e\mathbf{E}_e - e\mathbf{E}_h \\
 &= -\frac{e}{4\epsilon} \left( \frac{1}{\left(d + \frac{\mu}{m_e} r_{ex} \sin(\theta)\right)^2} + \frac{1}{\left(d - \frac{\mu}{m_h} r_{ex} \sin(\theta)\right)^2} \right. \\
 &\quad \left. - \frac{8 \left(2d + \frac{m_e - m_h}{m_e + m_h} r_{ex} \sin(\theta)\right)}{\left(r_{ex}^2 \cos^2(\theta) + \left(2d + \frac{m_e - m_h}{m_e + m_h} r_{ex} \sin(\theta)\right)^2\right)^{3/2}} \right) \hat{\mathbf{z}}
 \end{aligned} \tag{A2.10}$$

APPENDIX B

REFLECTION AND ANGLE DEPENDENT INTENSITY

For light exiting from a high index-of-refraction material to a lower index material, there will be an angle  $\theta_c$  at which light ceases to exit the material. All angles of emission greater than  $\theta_c$  will result in the total internal reflection of the emitted light back into the sample. Fig B.1 shows the critical angle and emission/internal reflection depending on whether  $\theta > \theta_c$  or  $\theta < \theta_c$ . In measuring the angle-dependent intensity of a sample, we must account for the fact that some portion of the light is internally reflected by the dielectric-air interface. Furthermore, we must keep in mind that, in our experiment, the angle of measurement is  $\theta'$  and not  $\theta$ . Therefore in the following equations we will use Snell's law to put  $\theta$  in terms of  $\theta'$ .



$$\theta = \sin^{-1}\left(\frac{n_{Air}}{n_{GaN}} \sin(\theta')\right) \quad (B.1)$$

In order to calculate the reflection coefficient at the boundary we will make use of Frensel equations, which allow us to calculate the reflection R as a function of the incident and transmitted angles, along with the indices of refraction of the

two materials involved. For s-polarized

Figure B.1 Schematic diagram of the path of a light ray from a source outwards at three angles:  $\theta$ ,  $\theta_c$  and  $>\theta_c$ . Only light emitted at  $\theta < \theta_c$  will be measured and be measured. The angle-dependent intensity measurement will see the light as having been emitted at angle  $\theta'$  instead of  $\theta$ .

light at the interface ( $E$  perpendicular to the plane-of-incidence) the reflection coefficient is:

$$\begin{aligned}
R_s &= \left( \frac{n_{GaN} \cos(\theta) - n_{Air} \cos(\theta')}{n_{GaN} \cos(\theta) + n_{Air} \cos(\theta')} \right)^2 \\
&= \left( \frac{n_{GaN} \sqrt{1 - \left(\frac{n_{Air}}{n_{GaN}}\right)^2 \sin^2(\theta')} - n_{Air} \cos(\theta')}{n_{GaN} \sqrt{1 - \left(\frac{n_{Air}}{n_{GaN}}\right)^2 \sin^2(\theta')} + n_{Air} \cos(\theta')} \right)^2 \\
&= \left( \frac{\frac{n_{GaN}}{n_{Air}} \sqrt{1 - \left(\frac{n_{Air}}{n_{GaN}}\right)^2 \sin^2(\theta')} - \cos(\theta')}{\frac{n_{GaN}}{n_{Air}} \sqrt{1 - \left(\frac{n_{Air}}{n_{GaN}}\right)^2 \sin^2(\theta')} + \cos(\theta')} \right)^2
\end{aligned} \tag{B.2}$$

Similarly, for p-polarized light ( $\mathbf{E}$  parallel to the plane-of-incidence) the reflection coefficient is:

$$\begin{aligned}
R_p &= \left( \frac{n_{GaN} \cos(\theta') - n_{Air} \cos(\theta)}{n_{GaN} \cos(\theta') + n_{Air} \cos(\theta)} \right)^2 \\
&= \left( \frac{n_{GaN} \cos(\theta') - n_{Air} \sqrt{1 - \left(\frac{n_{Air}}{n_{GaN}}\right)^2 \sin^2(\theta')}}{n_{GaN} \cos(\theta') + n_{Air} \sqrt{1 - \left(\frac{n_{Air}}{n_{GaN}}\right)^2 \sin^2(\theta')}} \right)^2 \\
&= \left( \frac{\cos(\theta') - \frac{n_{Air}}{n_{GaN}} \sqrt{1 - \left(\frac{n_{Air}}{n_{GaN}}\right)^2 \sin^2(\theta')}}{\cos(\theta') + \frac{n_{Air}}{n_{GaN}} \sqrt{1 - \left(\frac{n_{Air}}{n_{GaN}}\right)^2 \sin^2(\theta')}} \right)^2
\end{aligned} \tag{B.3}$$

In both cases we have used the relation  $\cos^2(\theta) = 1 - \sin^2(\theta)$  to allow us to use Eq. A3.1 to replace  $\theta$  by  $\theta'$ . Assuming that the QW has no preferred polarization for emission, we can construct the full reflection coefficient as simply  $R = (R_p + R_s)/2$ .

The externally measured intensity  $I'$  can then be related to the internal emission intensity  $I$  using the following relation:

$$I' = T(\theta') I = (1 - R(\theta')) I \quad (\text{B.4})$$

Therefore we can eliminate the effects of the angle dependent transmission/reflection by simply dividing the measured intensity  $I'$  by  $(1-R(\theta'))$ .

## REFERENCES

- [1] H. Wu, et al., *Photon. Tech. Lett.*, **17**, 1160 (2005).
- [2] J.K. Sheu, et al., *Photon. Tech. Lett.*, **15**, 18 (2003).
- [3] H. Amano, et al., in *Low Dimensional Nitride Semiconductors*, edited by B. Gil, (Oxford University Press, New York, 2002), pp. 105-120.
- [4] T. Fujii, et al., *Appl. Phys. Lett.*, **84**, 855 (2004).
- [5] E.M. Purcell, *Phys. Rev.*, **69**, 681 (1946).
- [6] A. Neogi, et al., *Phys. Rev. B* **66**, 153305 (2002).
- [7] N.E. Hecker, et al., *Appl. Phys. Lett.*, **75**, 1577 (1999).
- [8] C-Y. Cho, et al., *Nanotechnology*, **21**, 205201 (2010).
- [9] J.Y. Duboz, and J.C. Garcia, in *Low Dimensional Nitride Semiconductors*, edited by B. Gil, (Oxford University Press, New York, 2002), pp. 1-10.
- [10] V. Yu. Davydov, et al., *phys. stat. sol. (b)*, **230**, 2 R4-R6 (2002).
- [11] *NSM Archive – Physical Properties of Semiconductors*,  
<http://www.ioffe.ru/SVA/NSM/Semicond/index.html>
- [12] A. R. Denton, and N. W. Ashcroft, *Phys. Rev. A*, **43**, 3161 (1991).
- [13] A.G. Kontos, et al., *Phys. Rev. B*, **72**, 155336 (2005).
- [14] A. Hangleiter, et al., *Appl. Phys. Lett.*, **83**, 1169 (2003).
- [15] S. Tanaka, et al., *Appl. Phys. Lett.* **69**, 4096 (1996).
- [16] T. Paskova, and B. Monemar, in *Low Dimensional Nitride Semiconductors*, edited by B. Gil, (Oxford University Press, New York, 2002), pp. 79-104.
- [17] C. Trager-Cowan, et al., *Phys Rev B*, **75**, 085301 (2007)

- [18] I. Grzegory, and S. Porowski, in *Low Dimensional Nitride Semiconductors*, edited by B. Gil, (Oxford University Press, New York, 2002), pp. 57-78.
- [19] P. Ruterana, in *Low Dimensional Nitride Semiconductors*, edited by B. Gil, (Oxford University Press, New York, 2002), pp. 151-190.
- [20] A. Hangleiter, et al., *Phys. Rev. Lett.*, **95** 127402 (2005).
- [21] A. Llopis, et al., *IEEE J. Sel. Top. Quant. Elec.*, **15**, 1400 (2009).
- [22] S.F. Chichibu, et al., *Appl. Phys. Lett.*, **73**, 2006 (1998).
- [23] Y. Kawakami, in *Low Dimensional Nitride Semiconductors*, edited by B. Gil, (Oxford University Press, New York, 2002), pp. 233-256.
- [24] T. Kuroda, and A. Tackeuchi, *J. Appl. Phys.*, **92**, 3071 (2002).
- [25] Y.J. Wang, et al., *Optics Express*, **14**, 13151 (2006).
- [26] X.B. Zhang, and B. Gil, in *Low Dimensional Nitride Semiconductors*, edited by B. Gil, (Oxford University Press, New York, 2002), pp. 257-286.
- [27] O. Briot, et al., *phys. stat. sol. (c)*, **1**, 1420 (2004).
- [28] C. Kittel, *Introduction to Solid State Physics*, 8<sup>th</sup> ed., pp. 163-172 (Wiley, USA, 2005).
- [29] B. Gil, *Low Dimensional Nitride Semiconductors*, (Oxford University Press, New York, 2002).
- [30] J. Shah, *Ultrafast Spectroscopy of Semiconductors and Semiconductor Nanostructures*, 2<sup>nd</sup> Ed., (Springer, Germany, 1999).
- [31] R. Pecharroman-Gallego, *Semicond. Sci. Tech.* **22**, 1276 (2007).
- [32] A. Hangleiter, et al., *Philisophical Magazine*, **87**, 2041 (2007).
- [33] S. J. Rosner, et al., *Appl. Phys. Lett.*, **70**, 420 (1997)



- [34] L. Wang and N. C. Giles, *J. Appl. Phys.*, **94**, 973 (2003)
- [35] I. Robinson, and R., Harder, *Nature Materials* **8**, 291 (2009).
- [36] J. N. Chen, et al., *Nano Letters* **10**, 1280 (2010).
- [37] S.W. Lee, et al., *J. Phys. D: Appl. Phys.* **43**, 5 (2010).
- [38] L. Zhang, et al., *J. App. Phys.* **108**, 6 (2010).
- [39] X.B. Zhang, et al., *J. Phys. Condens. Matter* **13**, 7053 (2001).
- [40] J.J. Shi, *Phys. Rev. B* **68**, 165335 (2003).
- [41] V.Y. Davydov, et al., *J. App. Phys.* **82**, 5097 (1997).
- [42] X.Q. Wang, et al., *App. Phys. Lett.* **89**, 171907 (2006).
- [43] V. Darakchieva, et al., *Phys. Rev. B* **75**, 195217 (2007).
- [44] S. Kalliakos, et al., *Appl. Phys. Lett.* **80**, 428 (2002).
- [45] D. M. Graham, et al., *J. App. Phys.* **97**, 103508 (2005).
- [46] K. Huang, and A. Rhys, *Proc. R. Soc. London, Ser. A* **204** (1950).
- [47] W. Ungier and M. Suffczynski, *Phys Rev B*, **18**, 4390 (1978)
- [48] J. J. Shi, and Z. Z. Gan, *J. Appl. Phys.* **94**, 407-415 (2003).
- [49] J-Y Lu, et al., *J. Appl. Phys.* **108**, 123520 (2010).
- [50] V. Darakchieva, et al., *Appl. Phys. Lett.* **84**, 3636 (2004).
- [51] J. Cui and J. J. Shi, *Solid State Commun.* **145**, 235 (2008).
- [52] D. Chen, et al., *J. Appl. Phys.* **101**, 053712 (2007).
- [53] P.G. Moses, and C.G. Van de Walle, *Appl. Phys. Lett.* **96**, 021908 (2010).
- [54] V. Yu. Davydov, et al., *phys. stat. sol. (b)* **234**, 787 -795 (2002).
- [55] P. Gibart, *Rep. Prog. Phys.* **67**, 667 (2004).
- [56] J. S. Song, et al., *Phys. Rev. B* **81**, 233304 (2010).

- [57] K. Okamoto, et al., *Nature Mat.* **3**, 601 (2004).
- [58] J. Vučković, et al., *IEEE J. Quant. Elec.* **36**, 1131 (2000).
- [59] C-M. Wang, et al., *Opt. Express* **18**, 25608 (2010).
- [60] M-K. Kwon, et al., *Adv. Mater.* **20**, 1253 (2008).
- [61] S. Pereira, et al., *Adv. Mater.* **20**, 1038 (2008).
- [62] S. L. Chang, *Physics of Optoelectronic Devices*, (Wiley, New York, 1995).
- [63] Dai, Q., et al., *Appl. Phys. Lett.* **94**, 111109 (2009).
- [64] J. I. Climente, *J. Phys. Chem. C* **115**, 32, 15868 (2011).
- [65] I. Ho and G.B. Stringfellow, *Appl. Phys. Lett.* **69**, 2701 (1996).
- [66] S. Pereira et al., *Appl. Phys. Lett.* **81**, 1207 (2002).
- [67] Y-C. Cheng, et al., *Appl. Phys. Lett.* **84**, 2506 (2004).
- [68] J. A. Schuller, et al., *Nature Mat.*, **9**, 193 (2010).
- [69] Y.C. Jun, K. C. Y. Huang, and M. L. Brongersma, *Nature Comm.* **2**, 283 (2011).
- [70] T. V. Shubina, et al., *Phys. Rev. B* **82**, 073304 (2010).
- [71] J. B. You, et al., *J. Phys. D: Appl. Phys.* **41**, 20 (2008).
- [72] T. Chen, *Nanotechnology* **19**, 43 (2008).
- [73] K. W. Liu, et al., *Appl. Phys. Lett.* **94**, 151102 (2009).